# Cloud/shadow detection based on spectral indices for multi/hyperspectral optical remote sensing imagery

Han Zhai[a], Hongyan Zhang[a,b,*], Liangpei Zhang[a,b,*], Pingxiang Li[a,b]

[a] *The State Key Laboratory of Information Engineering in Surveying, Mapping and Remote Sensing, Wuhan University, Wuhan, Hubei 430079, PR China*
[b] *Collaborative Innovation Center of Geospatial Technology, Wuhan University, Wuhan, Hubei 430079, PR China*

## ARTICLE INFO

## ABSTRACT

Cloud and cloud shadow detection is a necessary preprocessing step for optical remote sensing applications because of the huge negative influence cloud and cloud shadow can have on data analysis. However, most of the existing cloud/shadow detection methods are designed based on specific band configurations of certain sensors, and their working mechanisms are relatively complex and computationally complicated, which limits their application. In view of this, in this paper, a unified cloud/shadow detection algorithm based on spectral indices (CSD-SI) is proposed for most of the widely used multi/hyperspectral optical remote sensing sensors with both visible and infrared spectral channels. On the one hand, the cloud index (CI) and cloud shadow index (CSI) are proposed to indicate the potential clouds and cloud shadows based on their physical reflective characteristics. In addition, considering the spatial coexistence of cloud and cloud shadow, a spatial matching strategy is utilized to remove the pseudo cloud shadows. The effectiveness of the proposed CSD-SI algorithm is demonstrated on eight different types of widely used multi/hyperspectral optical sensors, with different spectral and spatial resolution levels. Overall, in the experiments undertaken in this study, CSD-SI achieved a mean overall accuracy of 98.52% for cloud, with a mean producer's accuracy of 93.13% and a mean user's accuracy of 98.13%. For cloud shadow, CSD-SI achieved a means producer's accuracy of 84.33% and a mean user's accuracy of 89.12%. The experimental results show that the proposed CSD-SI method based on spectral indices can obtain a comparable cloud/shadow detection performance to that of the other state-of-the-art methods.

## 1. Introduction

Optical remote sensing images (such as Landsat/SPOT) are usually affected by clouds and their associated shadows (Dozier, 1989; Zhu and Woodcock, 2012; Zhu et al., 2015; Irish et al., 2006; Wu et al., 2016), which leads to disturbance and obstacles for Earth observation and can cause serious problems for various remote sensing applications, such as vegetation monitoring (Lu et al., 2017), land-cover/use analysis (Zhu and Woodcock, 2014), change detection (Zhu, 2017), and so on. Especially for quantitative analysis, the influence of clouds and their associated shadows is non-negligible with regard to the reliability of the conclusion. On the other hand, in many cases, acquiring a clear remote sensing image can consume a large amount of time, labor, and money. Hence, even if it is generally not possible to retrieve the missing information caused by cloud/shadow occlusion, it is still very important and necessary to accurately identify the cloud and cloud shadow in satellite images and screen them out before any kind of remote sensing application is performed.

Generally speaking, clouds are characterized by a higher reflectance and lower brightness temperature (BT) than other land materials (Platnick et al., 2003; Clerbaux et al., 2009; Zhu and Woodcock, 2012; Zhu et al., 2015; Sun et al., 2017), i.e., they generally appear white or gray in RGB space and dark in the thermal infrared band. However, it is not easy to accurately distinguish clouds from other bright land materials (such as rocks, bare soil, cement roads, and buildings) due to their similar reflective characteristics. In addition, the use of the thermal infrared band generally only works well for the thick, opaque clouds, and this approach obviously cannot be applied to the optical remote sensing sensors without this band, which limits its application field.

To date, many automatic cloud detection methods have been developed, which can be coarsely divided into two main categories: single-scene based methods and multi-scene based methods. In comparison, the multi-scene based methods are less popular although they generally have a higher detection accuracy than the single-scene based

---

methods (Goodwin et al., 2013; Jin et al., 2013; Lin et al., 2015) because of the utilization of the increased information offered by multitemporal images, i.e., at least two images over the same imaging area within a short period.

In 1976, "tasseled cap" (TC) transformation was first developed as a single-scene based mist or cloud detector (Kauth and Thomas, 1976). However, it fails to obtain satisfactory results in many cases as clouds and other materials do not strictly satisfy the simple TC orthogonal relationship assumption. Subsequently, Zhang et al. (2002) proposed the effective and notable "haze optimized transformation" (HOT) cloud detection algorithm by linearly regressing the blue and red bands to obtain a "clear-sky line", and utilized the distance to this line to separate clouds and other materials. Although HOT usually shows a better detection performance than TC, it often results in overestimation. The reason for this is that the HOT test often cannot effectively exclude other bright materials, such as rock and cement road (Zhu and Woodcock, 2012). In recent years, cloud detection algorithms based on machine learning have been developed, including Markov random field based methods (Le Hégarat-Mascle and André, 2009; Vivone et al., 2014; Li et al., 2018), neural network based methods (Hughes and Hayes, 2014), and support vector machine based methods (Li et al., 2015; Bai et al., 2016; Ishida et al., 2018), and have shown great potential. However, these methods generally have a high computational complexity and are time-consuming.

For cloud shadows, it is generally more difficult and challenging to effectively distinguish them from other dark land objects, such as water and topographical shadows (Zhu and Woodcock, 2012; Sun et al., 2018). This is because the reflective characteristics of these materials are very similar to those of cloud shadows. In addition, the reflective characteristics of cloud shadows are affected by the types of underlying land objects, to a large degree, which means that large spectral variability exists within cloud shadows. As a result, it is very difficult to accurately detect cloud shadows, and a large amount of noise can appear in the cloud shadow detection results.

With regard to cloud shadow detection, a large number of methods have been proposed, which can be coarsely divided into three main categories. The first category is based on projection law, and these methods utilize the sensor parameters (including the solar azimuth angle, solar altitude, and sensor altitude) as prior knowledge to calculate the projection direction of the cloud shadows (Simpson and Stitt, 1998). The second category is based on the use of the matched filter to identify the cloud shadows, which can be evaluated by the spectral band covariance matrix (Richter and Muller, 2005). The third category is spectral analysis combined with geometrical methods (Li et al., 2013), where geometrical operations are utilized to fill the gaps of the spectral tests. However, these approaches do not fully consider the large spectral variability of cloud shadows and the serious disturbance of dark pixels. Therefore, they generally fail to accurately detect cloud shadows.

In recent years, many cloud/shadow detection algorithms for specific satellite sensors have been proposed, especially for the Landsat series of sensors (Huang et al., 2010a,b; Roy et al., 2010). This is a result of the Landsat free-access policy and the fact that it is a valuable remote sensing data source for the observation and monitoring of the Earth's surface (Kennedy et al., 2010). For example, the classical automatic cloud cover assessment (ACCA) algorithm (Irish et al., 2006) was designed for the cloud cover assessment of Landsat 7 imagery. In recent works, the F-mask algorithm and its improved versions (Zhu and Woodcock, 2012; Zhu et al., 2015; Qiu et al., 2017) have been proposed for Landsat imagery and have obtained excellent cloud/shadow detection performances through a series of spectral tests and an object-based cloud and cloud shadow matching process. As a result, the F-mask algorithm and its improved versions have already been successfully used for practical applications with large amounts of Landsat images. However, many of the cloud/shadow detection algorithms designed for specific satellite sensors have some limitations, i.e., these algorithms

tend to select a low threshold in the detection procedure to identify all potential clouds, which generally leads to overestimation (Zhu et al., 2015). In addition, they are reliant on the thermal infrared band (Zhu and Woodcock, 2012; Qiu et al., 2017) or the cirrus band (Zhu et al., 2015), and hence cannot be effectively applied to other optical sensors (such as IKONOS) without the thermal infrared band or cirrus band.

An automatic multi-feature combined (MFC) method was recently proposed for the cloud and cloud shadow detection of Gaofen-1 (GF-1) wide field of view (WFV) imagery (Li et al., 2017). The MFC method first generates a preliminary cloud mask by threshold segmentation based on the spectral features and guided filtering. The geometric and textural features are then incorporated to improve the cloud detection result and produce the final cloud mask. The cloud shadow mask can be acquired by means of the cloud and shadow matching and the follow-up correction process. The MFC method can obtain an outstanding detection performance for GF-1 images.

However, to date, very few unified cloud/shadow detectors have been developed. Most of the existing methods are designed based on the specific band configurations of certain sensors and have limited generalizability. However, in many remote sensing applications, different remote sensing data sources must be simultaneously utilized (Zhu and Woodcock, 2012; Zhu et al., 2015), and it would take a lot of time and labor to select an appropriate cloud/shadow detection algorithm for each optical remote sensing sensor. Therefore, a unified cloud/shadow detection method, which can work well for various optical remote sensing sensors, is urgently required.

In view of this, in this paper, a unified cloud/shadow detection algorithm based on spectral indices (CSD-SI) is proposed for various multi/hyperspectral optical remote sensing sensors with both visible and infrared spectral channels. Firstly, based on the reflective characteristics of cloud and cloud shadow, the cloud index (CI) and cloud shadow index (CSI) are proposed for cloud and cloud shadow detection, respectively. These two indices are designed by integrating the visible and infrared spectra to fully consider the reflective characteristics of clouds and their associated shadows, which can effectively indicate the potential clouds and cloud shadows with few outliers, i.e., pseudo clouds or pseudo cloud shadows. Secondly, by fully considering the spatial coexistence of cloud and cloud shadow, a spatial matching strategy is utilized to remove the pseudo cloud shadows. The proposed CSD-SI algorithm is a unified cloud/shadow detection method for use with most of the widely used multi/hyperspectral optical remote sensing sensors with different spectral and spatial resolution levels. In other words, the proposed CSD-SI algorithm is not designed for specific sensors and is relatively robust to the channel designations of different sensors, as long as they include both visible and infrared bands. Furthermore, owing to the simple working mechanism, the proposed CSD-SI algorithm has a relatively low computational cost and makes sense for practical multi-source remote sensing applications.

The rest of this article is organized as follows. Section 2 describes the proposed cloud/shadow detection framework based on spectral indices (CSD-SI) in detail. Section 3 presents the experimental results. Section 4 discusses and analyzes the detection performance of the proposed algorithm in detail. Section 5 concludes the paper and hints at plausible future research lines.

## 2. Algorithm: Cloud/shadow detection based on spectral indices

In the remote sensing application field, spectral indices have been widely and successfully applied to various activities. Examples of the popular spectral indices are the normalized difference vegetation index (NDVI) for vegetation identification (Goward et al., 1991; Tucker et al., 2005; DeFries and Townshend, 1994), the normalized difference water index (NDWI) for water detection (Gao, 1996; McFeeters, 1996), and the normalized difference snow index (NDSI) for snow extraction (Dozier, 1989). Although these spectral indices are relatively simple, their performances are generally satisfactory, and they can usually meet
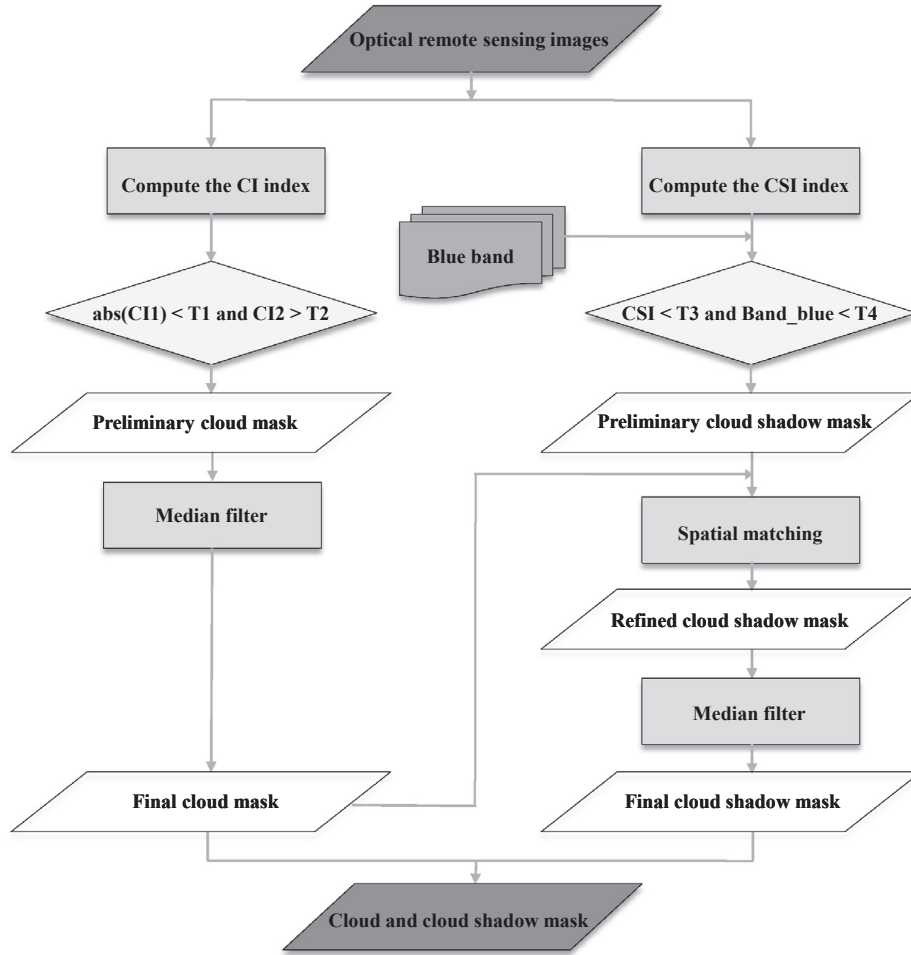
**Fig. 1.** The workflow of the proposed cloud/shadow detection algorithm based on spectral indices (CSD-SI).

the requirements of practical remote sensing applications, owing to their very low computational cost. Enlightened by the effectiveness of these spectral index based methods, a unified cloud/shadow detection algorithm based on spectral indices (CSD-SI) is proposed here. CSD-SI can simultaneously detect clouds and their associated shadows with a relatively high accuracy and low computational complexity, and it can work well for most of the widely used multi/hyperspectral optical remote sensing sensors with both visible and infrared spectral channels. As an overview, the workflow of the proposed CSD-SI algorithm is depicted in Fig. 1. A detailed introduction is given in the latter sections.

### 2.1. Cloud index and cloud detection

Generally speaking, cloud has its own reflective characteristics in optical remote sensing images. Indeed, the brightness of cloud-contaminated regions increases with a relatively large magnitude in the visible, near-infrared (NIR), and short wave infrared (SWIR) bands. This means that the digital number (DN) values of cloud pixels are much larger than those of other materials in these bands, especially for thick clouds. Meanwhile, cloud pixels also have similar reflective characteristics in the visible and infrared bands, which are commonly different from other land-cover materials, as shown in Fig. 2.

Based on the aforementioned reflective characteristics, the CI index is proposed to distinguish clouds from other land materials. Most of the widely used moderate/low-resolution multi/hyperspectral remote sensing sensors have both NIR spectral channels and SWIR spectral channels, but the high-resolution sensors commonly only feature the NIR spectral channel. According to whether or not the SWIR bands are

included, the CI index can be alternatively formulated as the following two forms:

$$CI_1 = \frac{\mathbf{B}_{NIR} + 2 \times \mathbf{B}_{SWIR-1}}{\mathbf{B}_B + \mathbf{B}_G + \mathbf{B}_R} \ \ or \ \ CI_1 = \frac{3 \times \mathbf{B}_{NIR}}{\mathbf{B}_B + \mathbf{B}_G + \mathbf{B}_R} \tag{1-a}$$

$$CI_2 = (\mathbf{B}_B + \mathbf{B}_G + \mathbf{B}_R + \mathbf{B}_{NIR} + \mathbf{B}_{SWIR-1} + \mathbf{B}_{SWIR-2})/6 \ \ or \ \ CI_2$$
$$= (\mathbf{B}_B + \mathbf{B}_G + \mathbf{B}_R + \mathbf{B}_{NIR})/4 \tag{1-b}$$

where $\mathbf{B}_B$, $\mathbf{B}_G$, and $\mathbf{B}_R$ denote the blue, green, and red bands, respectively, which are in the visible range. $\mathbf{B}_{NIR}$, $\mathbf{B}_{SWIR-1}$, and $\mathbf{B}_{SWIR-2}$ denote the three infrared bands: the NIR band, the SWIR band with a shorter wavelength, and the SWIR band with a longer wavelength, respectively.

In Eq. (1-a), the $CI_1$ index, i.e., the ratio of the sum of the infrared bands and the sum of the visible bands, is utilized to measure the similarity of the reflective characteristics in the visible bands and the infrared bands. Generally speaking, considering that clouds usually have similar reflective properties in the visible bands and the infrared bands, the $CI_1$ index usually lies in a very narrow range around 1. In Eq. (1-b), the $CI_2$ index, i.e., the mean of all the related spectral bands, is constructed to describe the brightness property of clouds. The clouds can be effectively detected with the following formulation:

$$(|\mathbf{CI}_1 - 1| < T_1) \ or \ (\mathbf{CI}_2 > T_2) \tag{2}$$

where $T_1$ is a small threshold and $T_2$ is a large threshold, which are explained in detail in Section 2.3. From the theoretical perspective, through combining these two identification criteria, the clouds in the images can be detected, with the disturbance factors caused by other bright land materials such as rock, bare soil, and cement road excluded,
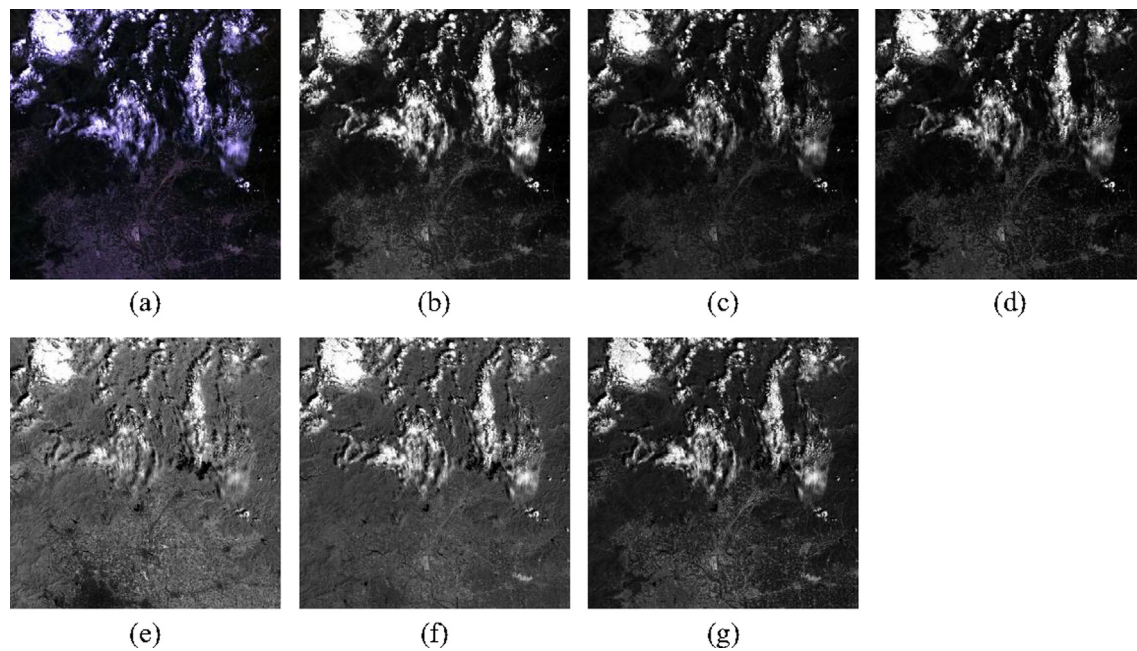
**Fig. 2.** A cloud-contaminated image of the Landsat 5 TM sensor. (a) True RGB image. (b) Blue band image. (c) Green band image. (d) Red band image. (e) Near-infrared band image. (f) Short wave infrared band image with shorter wavelength. (g) Short wave infrared band image with longer wavelength. (For interpretation of the references to color in this figure legend, the reader is referred to the web version of this article.)

as few land materials simultaneously satisfy both the $\mathbf{CI}_1$ and $\mathbf{CI}_2$ constraints.

### 2.2. Cloud shadow index and cloud shadow detection

Compared with cloud detection, cloud shadow detection is more complex and difficult (Le Hégarat-Mascle and André, 2009; Zhu and Woodcock, 2012; Zhu et al., 2015). The reason for this is that cloud shadow can be cast on any kind of land object, and the DN values only partly reflect the characteristics of cloud shadow. This means that the reflective characteristics of cloud shadow are highly dependent on the underlying land objects. Hence, an effective detection rule is not easy to define. In addition, the reflective characteristics of some dark land objects (such as water and topographical shadow) are very similar to those of cloud shadow, which makes it a challenging task to accurately separate cloud shadow from other land objects.

Firstly, using the same strategy as cloud detection, an effective spectral index should be designed with the most representative and distinguishable spectral channels to indicate potential cloud shadows. A widely used prior for cloud shadows is that cloud shadows are mainly illustrated by scattered light as beam solar radiation is blocked by clouds (Zhu and Woodcock, 2012). Furthermore, atmospheric scattering is stronger in the shorter wavelengths, i.e., the visible bands, and the diffusive radiation in shadows is weaker in the longer wavelengths, i.e., the NIR and SWIR bands, leading to cloud shadows being darker than their surroundings (Luo et al., 2008; Zhu and Woodcock, 2012; Zhu et al., 2015). On the other hand, many kinds of land objects have a relatively high reflectance in the NIR and SWIR bands, including vegetation, rock, and bare soil, which makes the darkening effect of cloud shadows more obvious in these bands. In addition, the NIR band is widely utilized in cloud shadow detection and has been verified to be effective (Le Hégarat-Mascle and André, 2009; Zhu and Woodcock, 2012; Zhu et al., 2015; Qiu et al., 2017; Li et al., 2017). Therefore, the NIR band is utilized to detect cloud shadow in our work, and in order to further enhance the difference between cloud shadow and other materials, the SWIR-1 band is also utilized together with the NIR band to design the cloud shadow indicator. The SWIR-2 band is not included, because of its relatively large difference in spectral range compared

with the other bands.

Based on the aforementioned reflective characteristics, the CSI index is proposed to detect the cloud shadows contained in optical images. Similar to the CI index, according to whether or not the SWIR-1 band is included, the CSI index can be alternatively constructed as the following two formulations:

$$\mathbf{CSI} = (\mathbf{B}_{NIR} + \mathbf{B}_{SWIR-1})/2 \;\; or \;\; \mathbf{CSI} = \mathbf{B}_{NIR} \tag{3}$$

where the CSI index is designed as the mean of the NIR band and the SWIR-1 band, or only the NIR band, and is utilized to denote the reflective properties of cloud shadow in the longer wavelengths. However, water usually has similar very dark characteristics in these bands, and some other constraints need to be added to exclude water and identify the cloud shadows cast on water. With consideration of the relatively high reflectance of water in the shorter wavelengths, i.e., the blue band, the blue band is utilized to exclude water. With these two spectral tests, the cloud shadow can be identified as follows:

$$(\mathbf{CSI} < T_3) \;\; and \;\; (\mathbf{B}_B < T_4) \tag{4}$$

where $T_3$ and $T_4$ are small thresholds, which are explained in detail in Section 2.3.

However, in many cases, topographical shadows cannot be absolutely excluded only with these spectral tests, as they have very similar reflective characteristics to cloud shadows. As is known to us all, cloud shadows are generated by cloud occlusion. That is to say, clouds and cloud shadows should show spatial coexistence (Le Hégarat-Mascle and André, 2009; Zhu and Woodcock, 2012; Zhu et al., 2015). Based on this fact, the spatial coexistence can be incorporated to remove the pseudo cloud shadows and refine the detection result. Specifically, the coarse cloud shadow detection result obtained by the CSI test can be pixel-wise refined by the spatial matching strategy. This strategy involves searching for cloud pixels in the local spatial neighborhood of each potential cloud shadow pixel, to determine whether it is a real cloud shadow pixel or not. If some cloud pixels exist within the local neighborhood, the potential cloud shadow pixels are finally determined as real ones. Otherwise, they are determined as pseudo cloud shadow pixels and removed. In this way, the disturbances caused by topographical shadows can be effectively relieved and the cloud shadow

detection result can be refined.

On the other hand, clouds and cloud shadows actually have a precise geometric relationship (Le Hégarat-Mascle and André, 2009; Zhu and Woodcock, 2012; Zhu et al., 2015), in that cloud shadows are always present along a certain direction to clouds, according to geometrical projection law. In practice, the spatial searching process is only needed on one side of the shadows for a certain imaging scene. In our study, a rectangular local window is utilized to flexibly control the search range. The process of cloud shadow detection is depicted in Fig. 3.

With the CI and CSI indices, the proposed CSD-SI algorithm can effectively detect clouds and their associated shadows at the same time. Through the spatial matching strategy, the pseudo cloud shadows, i.e., the topographical shadows, can be removed. A median filter is then utilized as a post-processing step for the cloud detection map and cloud shadow detection map, respectively, to further remove the noise and refine the detection results. Finally, the refined cloud detection map and cloud shadow detection map are combined to generate the cloud/shadow detection thematic map. The proposed CSD-SI algorithm is summarized in Algorithm 1.

---

**Algorithm 1.** The Proposed CSD-SI Algorithm for Cloud/Shadow Detection of Multi/Hyperspectral Optical Remote Sensing Images

---

**Input data:** the original multi/hyperspectral optical remote sensing image.

**Main algorithm:**

(1) Cloud detection:

    Mask clouds according to Eq. (2) with the CI spectral index defined in Eq. (1);

    Conduct post-processing with the median filter to remove noise/outliers and refine the detection result to obtain the final cloud detection result.

(2) Cloud shadow detection:

    Mask all the potential cloud shadows according to Eq. (4) with the CSI spectral index defined in Eq. (3);

    Refine the cloud shadows with spatial matching with the help of the cloud detection result;

    Conduct post-processing with the median filter to remove noise/outliers and further refine the detection result to obtain the final cloud shadow detection result.

(3) Cloud/shadow detection:

    Combine the refined cloud detection map and cloud shadow detection map to generate the final cloud/shadow detection thematic map.

**Output result:** the cloud/shadow detection thematic map.

---

### 2.3. Parameter setting

In the proposed CSD-SI algorithm, there are eight parameters: four threshold parameters for the spectral tests, two size parameters for the local search window, and two kernel size parameters for the median filter. In this section, the sensitivity of each parameter is first theoretically analyzed. The parameter setting rules are then described in detail.

#### 2.3.1. Theoretical analysis of parameter sensitivity

$T_1$ is a threshold parameter of the $CI_1$ index in the cloud detection, and is utilized to constrain the similarity of the reflective characteristics of clouds in the visible and infrared bands. If $T_1$ is set too large, e.g., more than 10, the exclusion power will be weakened, which may result in more outliers caused by other bright land-cover materials and an increment of the commission rate. On the other hand, if $T_1$ is set too small, e.g., less than 0.1, the detection capability will be limited and

many clouds will be missed, which will lead to an increase of the omission rate.

$T_2$ is a threshold parameter of the $CI_2$ index in the cloud detection, and is utilized to constrain the brightness property of clouds. As clouds are usually brighter than other land materials, $T_2$ is generally set as a relatively large value. Even for the thin cirrus clouds which may not be so bright, their reflectance is still higher than clear-sky pixels. Generally speaking, a smaller $T_2$ leads to more clouds being detected, but will also result in larger commission errors. Conversely, a larger $T_2$ can better screen out the outliers caused by other bright land-cover materials, but will lead to larger omission errors.

$T_3$ is a threshold parameter of the $CSI$ index in the cloud shadow detection, which is used to describe the dark property of cloud shadows. $T_3$ is generally set as a relatively small value. In general, a larger $T_3$ leads to more cloud shadows being detected, but will lead to larger commission errors, while a smaller $T_3$ will miss many of the cloud shadows, but will guarantee lower commission errors.

$T_4$ is a threshold parameter to remove the influence of water in the cloud shadow detection process, and is generally set as a relatively small value. Similarly, a smaller $T_4$ can better exclude the influence of water, but will also lead to a higher omission rate.

$T_5$ and $T_6$ are two size parameters for the height and width of the local search window, which are utilized to control the spatial search range in the cloud/shadow matching procedure. If $T_5$ and $T_6$ are set as small values, many real cloud shadows will be missed. If they are set as larger values, the time consumption will become greater. Therefore, a tradeoff should be determined between the accuracy and the time consumption in practice.

$T_7$ and $T_8$ are two kernel size parameters of the median filters for cloud and cloud shadow, which are utilized to control the smoothing strength of noise. Generally speaking, larger values of $T_7$ and $T_8$ can better filter out the noise, but will lead to some deterioration in the cloud and cloud shadow detection effects.

#### 2.3.2. Parameter setting rules

In order to make the CSD-SI algorithm convenient and practical for real remote sensing applications, recommended values and formulations for the parameters are given in the following. Without special instructions, $\min(\cdot)$, $\text{mean}(\cdot)$, and $\max(\cdot)$ refer to the minimum, mean, and maximum value of a synthetic band, i.e., $CI_2$ and $CSI$, or a specific band, i.e., blue band ($B_B$), respectively. Although these values are image-related, they can be easily and automatically calculated for a certain image. This means that, for any optical remote sensing sensor with both visible and infrared bands, these values can be easily obtained according to the formulations and the recommended values. Hence, these values do not affect the generalizability and practicability of the proposed CSD-SI algorithm.

For the first parameter $T_1$, it is generally set as a small value, e.g., 1. The value of $T_1$ is selected from the set of {0.01, 0.1, 1, 10, 100} and can be easily fine-tuned for particular image scenes through a few experiments.

Parameter $T_2$ is always set as a large value. Considering the reflective characteristics of various land-cover objects, in practice, $T_2$ can be adaptively determined as follows:

$$T_2 = \text{mean}(CI_2) + t_2 \times (\max(CI_2) - \text{mean}(CI_2)) \quad (5)$$

where $t_2 \in (0, 1)$ is an adjusting coefficient, which is generally selected from the set of {1/10, 1/9, 1/8, 1/7, 1/6, 1/5, 1/4, 1/3, 1/2}.

The third parameter $T_3$ is generally set as a small value. Similarly, it can be obtained as follows:

$$T_3 = \min(CSI) + t_3 \times (\text{mean}(CSI) - \min(CSI)) \quad (6)$$

where $t_3 \in (0, 1)$ is an adjusting coefficient, which is generally selected from the set of {1/4, 1/3, 1/2, 2/3, 3/4}.

The fourth parameter $T_4$ is generally set as a small value. In practice, it can be determined as follows:
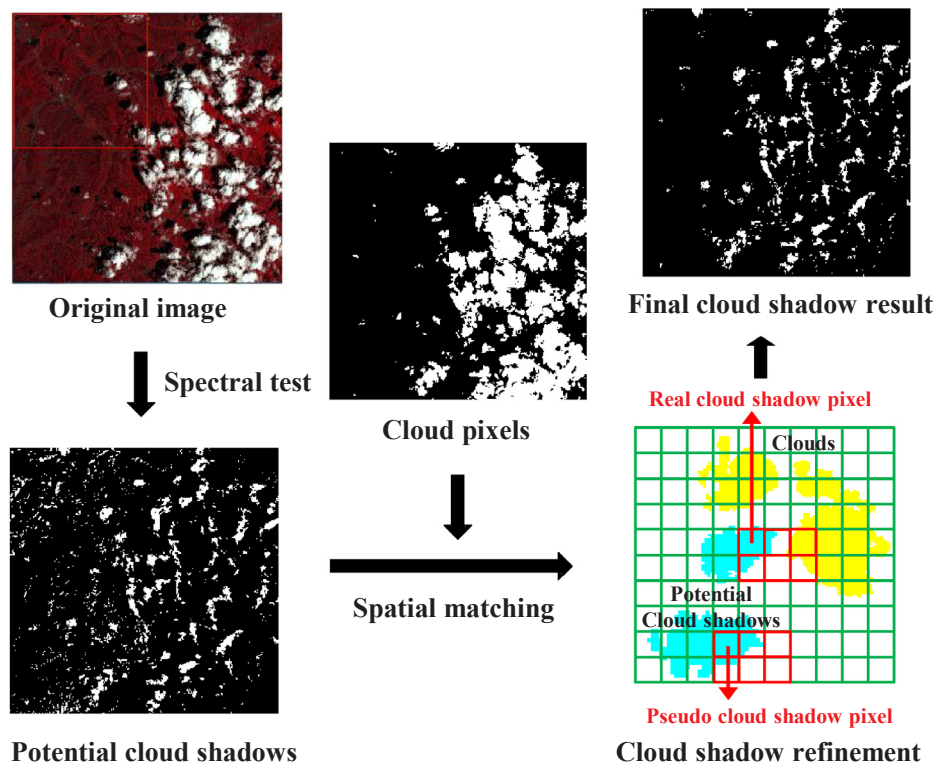
**Fig. 3.** The process of cloud shadow detection.

$$T_4 = \min(\mathbf{B}_B) + t_4 \times (\text{mean}(\mathbf{B}_B) - \min(\mathbf{B}_B)) \qquad (7)$$

where $t_4 \in (0, 1)$ is an adjusting coefficient, which is generally selected from the set of $\{1/2, 2/3, 3/4, 4/5, 5/6\}$.

The fifth and sixth parameters, $T_5$ and $T_6$, are size parameters to control the height and width of the local search window in the spatial matching procedure. Although these two parameters need to be estimated for each scene, the determination process is not complex. Generally speaking, the magnitude of the two parameters can be coarsely determined by visual estimation according to the relative distance between the clouds and their associated shadows. These two parameters can then be easily fine-tuned for particular image scenes through a few experiments.

The seventh and eighth parameters, $T_7$ and $T_8$, are generally selected from the set of $\{3, 5, 7, 9, 11\}$ and can be coarsely determined by the spectral index detection efficacy. Then, through fine-tuning, the optimal values can be easily obtained.

In general, the parameters of the proposed CSD-SI algorithm are fewer than those of the other state-of-the-art cloud/shadow detection algorithms. For example, the ACCA algorithm has 35 parameters, including 32 fixed parameters with recommended values and three dynamic parameters (Irish et al., 2006). In addition, the optimal values of the proposed CSD-SI algorithm parameters can be easily obtained through fine-tuning according to the formulations and the recommended values, which suggests that the proposed CSD-SI algorithm makes sense for real remote sensing applications.

### 2.4. CSD-SI: Comparison with other algorithms

In order to illustrate the performance of the proposed CSD-SI algorithm, the mean cloud/shadow detection precisions are compared with those of five other well-known state-of-the-art cloud/shadow detection algorithms: the ACCA algorithm (Irish et al., 2006) and F-mask algorithm (Zhu and Woodcock, 2012) for Landsat images, the improved F-mask based on cloud displacement index (F-mask-CDI) (Frantz et al., 2018) for Sentinel 2 image, the machine learning and multi-feature

fusion (MLMFF) method (Bai et al., 2016) and MFC (Li et al., 2017) for GF-1 images. The detection precision comparisons and analysis are given in Section 4.2.

### 3. Experimental tests: Performance and analysis

To thoroughly evaluate the performance of the proposed CSD-SI algorithm, the three main kinds of optical remote sensing sensors were selected, i.e., multispectral, high-resolution, and hyperspectral. For each kind of optical sensor, some of the most widely used and representative satellite sensors were selected. Specifically, for the multispectral sensors, the three Landsat series sensors (Thematic Mapper (TM), Enhanced Thematic Mapper Plus (ETM+), and Operational Land Imager (OLI)) and Sentinel-2 were selected. For the high-resolution optical sensors, GF-1 and IKONOS were selected. For the hyperspectral sensors, MODIS and Hyperion were selected. Correspondingly, eight different remote sensing image scenes under different geographical environments with different cloud types were selected as the validation datasets, with various spectral and spatial resolution levels. The cloud amounts varied from approximately 10% to 80%. The spatial resolutions ranged from kilometers to meters, and the spectral channels varied from four to hundreds. Meanwhile, the most commonly used accuracy assessment metrics were adopted to conduct the quantitative evaluations based on the reference maps, which were manually drawn via visual inspection by experienced users (Zhu and Woodcock, 2012; Zhu et al., 2015; Li et al., 2017; Bai et al., 2016). It is worth mentioning that all the cloud and cloud shadow pixels of each experimental image were carefully labeled by experienced users, which could guarantee the reliability of the quantitative assessment.

In the following, for cloud, three accuracies are provided (the overall accuracy (OA), producer's accuracy (PA), and user's accuracy (UA)), by considering cloud and non-cloud as two classes. For cloud shadow, two accuracies are given (PA and UA), by considering cloud shadow and non-cloud shadow as two classes. These five accuracies are formulated as follows (Zhu and Woodcock, 2012; Qiu et al., 2017):
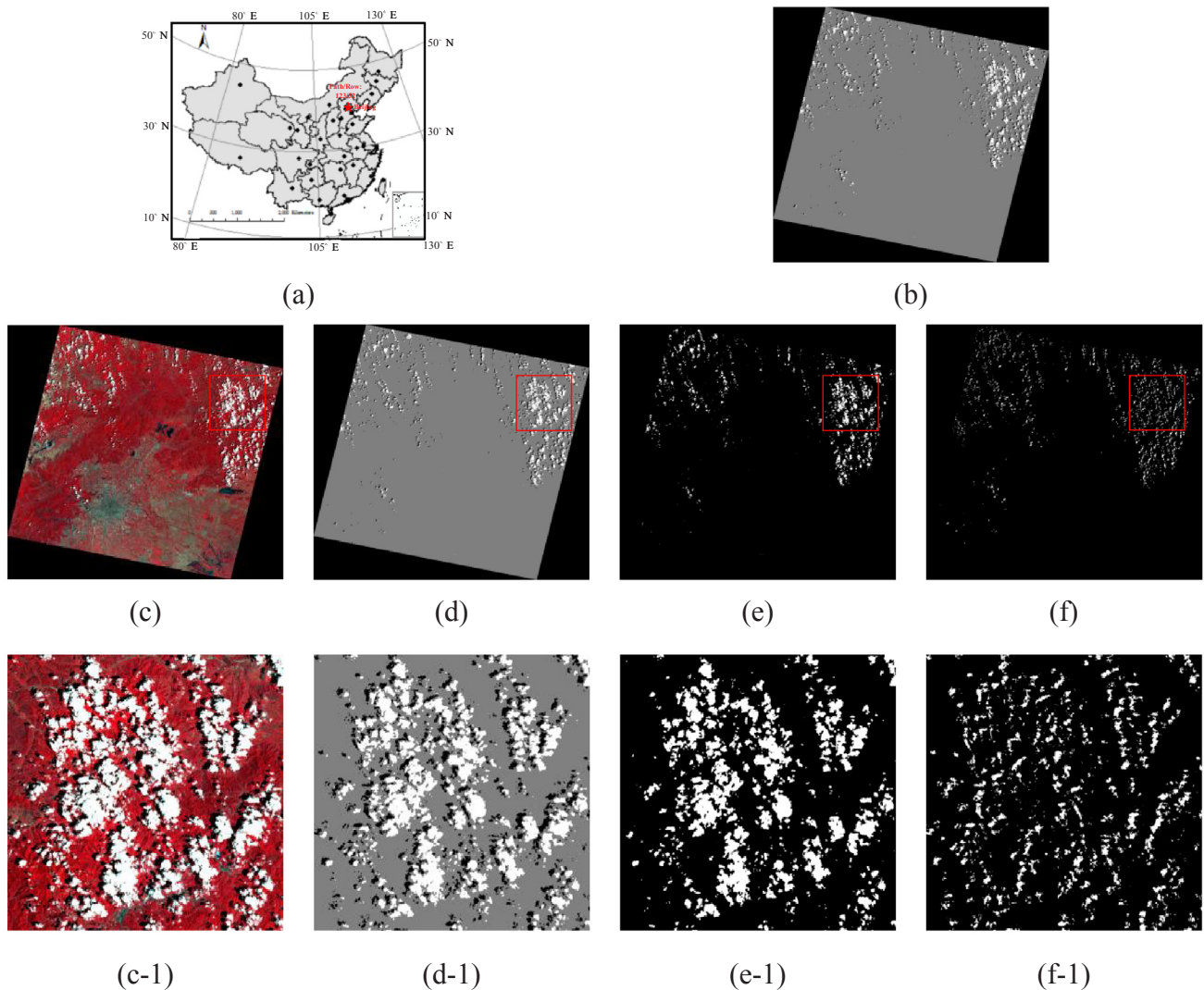
(a)

(b)

(c)

(d)

(e)

(f)

(c-1)

(d-1)

(e-1)

(f-1)

**Fig. 4.** Beijing Landsat 5 TM image scene (path/row 123/32) and the cloud/shadow detection results of the proposed CSD-SI detection algorithm: (a) The geographical location of the covered area. (b) The reference map. (c) The false-color composite image of Beijing (R: 4, G: 3, B: 2). (d) The composite cloud/shadow thematic map. (e) The cloud detection map. (f) The cloud shadow detection map. (c-1)–(f-1) Local zoomed maps of the detection results labeled with the red square in (c) to (f). (For interpretation of the references to color in this figure legend, the reader is referred to the web version of this article.)

$$Cloud\ OA = \frac{agreement\ bewteen\ cloud\ reference\ map\ and\ detection\ result}{total\ pixels}$$

(8-a)

$$Cloud\ PA = \frac{agreement\ of\ cloud}{agreement\ of\ cloud + omission\ of\ cloud}$$

(8-b)

$$Cloud\ UA = \frac{agreement\ of\ cloud}{agreement\ of\ cloud + comission\ of\ cloud}$$

(8-c)

$$Cloud\ shadow\ PA = \frac{agreement\ of\ cloud\ shadow}{agreement\ of\ cloud\ shadow + omission\ of\ cloud\ shadow}$$

(8-d)

$$Cloud\ shadow\ UA = \frac{agreement\ of\ cloud\ shadow}{agreement\ of\ cloud\ shadow + comission\ of\ cloud\ shadow}$$

(8-e)

### 3.1. Case study: Landsat 5 TM image

#### 3.1.1. Experimental setting

The first real-data experiment was conducted on a multispectral image of Beijing (path/row 123/32) acquired by the Landsat 5 TM sensor on July 6th, 2004. Beijing is situated in the northern part of China and belongs to the northern hemisphere mid-latitude region (see Fig. 4(a)). The reference map of the cloud and cloud shadow for this scene is provided in Fig. 4(b). In this scene, there are both mountain and plain regions. The clouds in this image mainly consist of thick, opaque clouds, and are mainly distributed in the upper part of the image, which can be seen from the false-color composite image in Fig. 4(c). This scene is relatively challenging for cloud and cloud shadow detection because there are significant disturbances in the scene, including bright cement roads, rocks, dark water, topographical shadows, and so on. The parameters of the proposed CSD-SI algorithm were set as: $T_1 = 1$, $t_2 = 1/3$, $t_3 = 1/2$, $t_4 = 5/6$, $T_5 = 40$, $T_6 = 50$, $T_7 = 7$, and $T_8 = 3$, which were fine-tuned to be optimal through a few experiments.

#### 3.1.2. Results

The detection maps of the proposed CSD-SI algorithm, i.e., the cloud detection map, the cloud shadow detection map, and the composite cloud/shadow detection thematic map, are shown in Fig. 4(d)–(f). In order to better demonstrate the detection performance, both the whole image scene detection maps and local zoomed maps are provided.
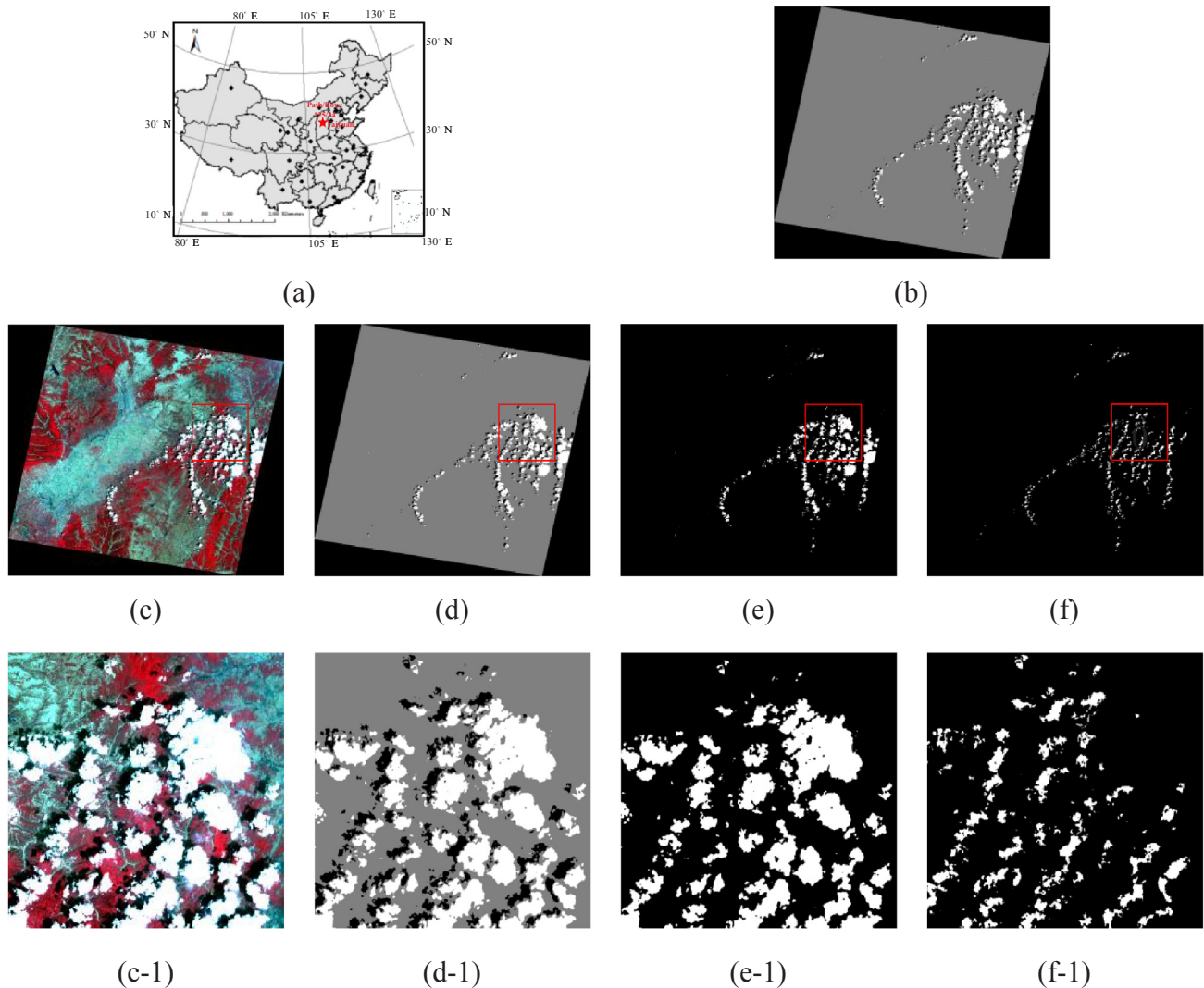
**Fig. 5.** Taiyuan Landsat 7 ETM+ image scene (path/row 125/34) and the cloud/shadow detection results of the proposed CSD-SI detection algorithm: (a) The geographical location of the covered area. (b) The reference map. (c) The false-color composite image of Taiyuan (R: 4, G: 3, B: 2). (d) The composite cloud/shadow thematic map. (e) The cloud detection map. (f) The cloud shadow detection map. (c-1)–(f-1) Local zoomed maps of the detection results labeled with the red square in (c) to (f). (For interpretation of the references to color in this figure legend, the reader is referred to the web version of this article.)

From Fig. 4, it can be seen that the proposed CSD-SI algorithm achieves a good performance in this scene. From the whole scene maps, it can be observed that the clouds and cloud shadows are relatively accurately identified, with the outliers caused by other bright materials and dark topographical shadows well screened out. Specifically, both the large cloud groups and their associated cloud shadows, e.g., in the upper-right part of the image, and the small isolated clouds and cloud shadows, e.g., in the upper-middle part of the image, are effectively detected. From the local zoomed maps, it can be noted that the detected clouds and their associated cloud shadows are basically consistent with the false-color image, from a visual evaluation. Furthermore, the shapes and spatial positions of the clouds and their associated shadows are relatively well maintained, with the edges and the internal structural details well described, which verifies the effectiveness of the proposed CSD-SI algorithm. In general, nearly all the potential clouds and cloud shadows are effectively detected, which suggests the effectiveness of the proposed CI and CSI indices. Moreover, with the help of the spatial matching strategy, the cloud shadow detection result is further refined by removing the pseudo cloud shadows without any accompanying clouds. However, from the local zoomed maps, it can be found that some very small clouds are missed, accounting for approximately 9.3%,

and some pseudo cloud shadows still exit in the detection maps, accounting for approximately 14.51%.

### 3.2. Case study: Landsat 7 ETM+ image

#### 3.2.1. Experimental setting

The second experiment was conducted on a multispectral image collected by the Landsat 7 ETM+ sensor over the city of Taiyuan (path/row 125/34) on May 21st, 2014. Taiyuan is also located in the northern part of China and is a typical landlocked city (see Fig. 5(a)). Similarly, both mountain and plain regions are included in the scene. The clouds mainly consist of thick, opaque clouds and mainly concentrate in the right part of the scene, with large cloud groups surrounded by many small clouds, which is difficult for accurate detection. The reference map and the composite false-color image are given in Fig. 5(b) and (c), respectively. The parameters in this scene were set as: $T_1 = 1$, $t_2 = 1/2$, $t_3 = 1/2$, $t_4 = 3/4$, $T_5 = 80$, $T_6 = 70$, $T_7 = 9$, and $T_8 = 5$, which were fine-tuned to be optimal through a series of experiments.

#### 3.2.2. Results

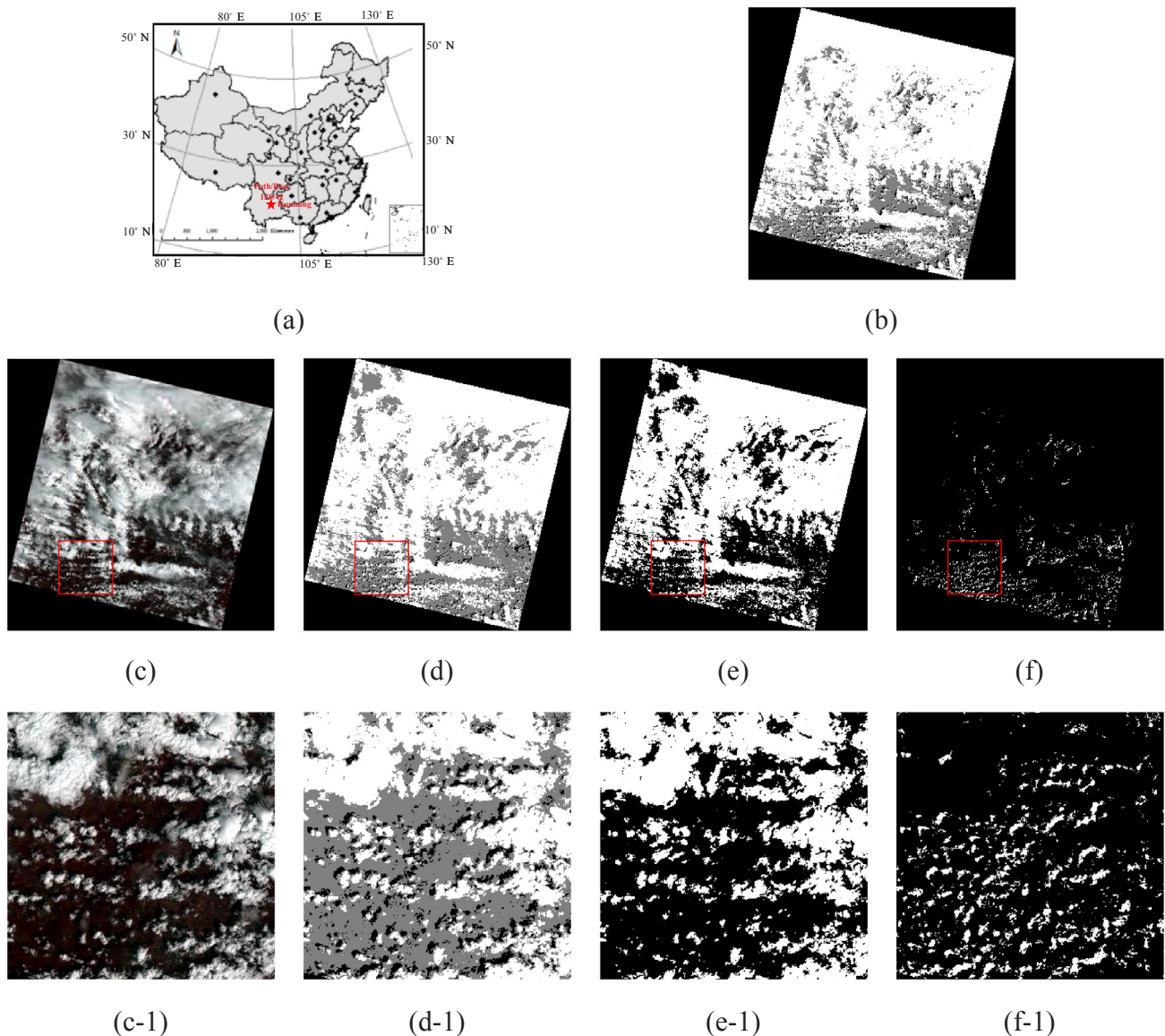The cloud/shadow detection maps of the proposed CSD-SI algorithm

**Fig. 6.** Kunming Landsat 8 OLI image scene (path/row 129/42) and the cloud/shadow detection results of the proposed CSD-SI detection algorithm: (a) The geographical location of the covered area. (b) The reference map. (c) The false-color composite image of Kunming (R: 5, G: 4, B: 3). (d) The composite cloud/shadow thematic map. (e) The cloud detection map. (f) The cloud shadow detection map. (c-1)–(f-1) Local zoomed maps of the detection results labeled with the red square in (c) to (f). (For interpretation of the references to color in this figure legend, the reader is referred to the web version of this article.)

are shown in Fig. 5(d)–(f). Again, both the whole image scene detection maps and local zoomed maps are provided to demonstrate the detection performance. By comprehensively analyzing Fig. 5, it can be found that the experimental results in this scene are consistent with those of the first experiment, and similar conclusions can be drawn. The proposed CSD-SI algorithm performs well in this scene by effectively detecting the clouds and cloud shadows and relieving the disturbances caused by other land materials with similar spectral responses, thereby achieving a relatively good detection result. For example, the large cloud groups and the surrounding small, isolated clouds in the right-middle part of the image are well described in the detection results. From the whole scene maps, it can be seen that the detected clouds and cloud shadows are basically consistent with the false-color image, and from the local zoomed maps, it can be observed that the shapes and spatial positions of the clouds and cloud shadows are relatively well maintained, with the boundaries and internal structural details relatively well described, except for a few omissions of cloud shadows, accounting for approximately 19.47%, which further demonstrates the effectiveness of the proposed CSD-SI algorithm.

### 3.3. Case study: Landsat 8 OLI image

#### 3.3.1. Experimental setting

The third real-data experiment was conducted on a multispectral image of the city of Kunming (path/row: 129/42) obtained by the Landsat 8 OLI sensor on March 30th, 2017. Kunming is located in the southern part of China (see Fig. 6(a)) and has a typical subtropical climate. Unlike the first two scenes, this scene is a much more complex case with a lot of thin clouds around the thick, opaque clouds, and the cloud amount is over 80%, covering most areas of the image, which further increases the challenge for the cloud/shadow detection task. The reference map and the false-color composite image are provided in Fig. 6(b) and (c), respectively. The parameters in this scene were set as: $T_1 = 1$, $t_2 = 1/10$, $t_3 = 1/3$, $t_4 = 1/2$, $T_5 = 100$, $T_6 = 150$, $T_7 = 3$, and $T_8 = 3$, which were fine-tuned to be optimal through several experiments.

#### 3.3.2. Results

The cloud/shadow detection maps of the proposed CSD-SI algorithm are shown in Fig. 6(d)–(f). From Fig. 6, it can be observed that some
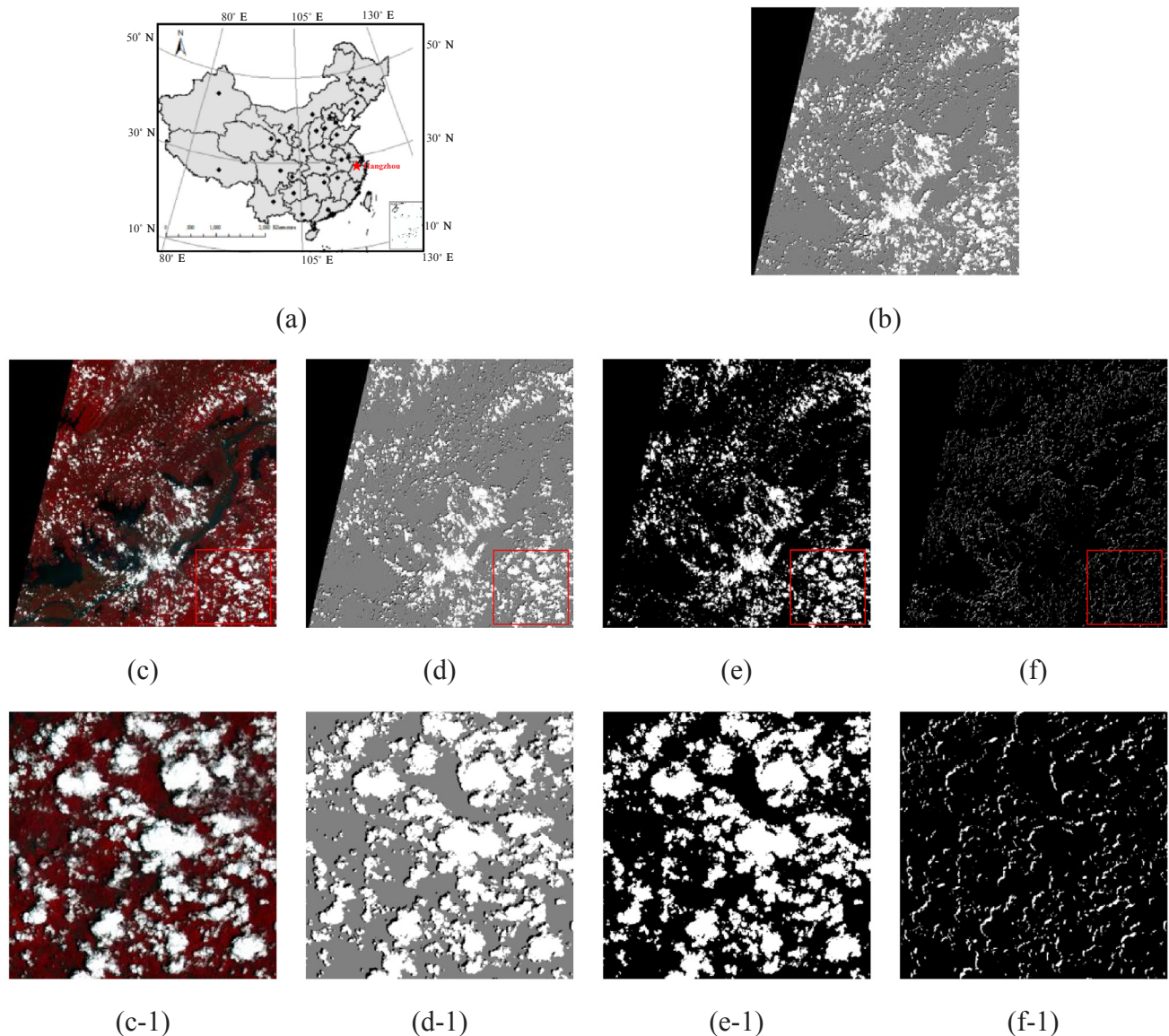
**Fig. 7.** Hangzhou Sentinel-2 image scene and the cloud/shadow detection results of the proposed CSD-SI detection algorithm: (a) The geographical location of the covered area. (b) The reference map. (c) The false-color composite image of the acquired Hangzhou Sentinel-2 image scene (R: 8, G: 3, B: 2). (d) The composite cloud/shadow thematic map. (e) The cloud detection map. (f) The cloud shadow detection map. (c-1)–(f-1) Local zoomed maps of the detection results labeled with the red square in (c) to (f). (For interpretation of the references to color in this figure legend, the reader is referred to the web version of this article.)

very thin clouds around the thick, opaque clouds are not detected, accounting for approximately 10.39%, especially for the upper-left part of the image, which limits the detection performance, to some degree. However, in general, the proposed CSD-SI algorithm still achieves an acceptable detection performance by effectively identifying most of the clouds together with their associated shadows, and screening out the noise and disturbances. From both the whole scene maps and the local zoomed maps, it can be observed that most parts of the cloud detection map and cloud shadow detection map are basically consistent with the false-color image, from a visual evaluation, with the edges and details of the clouds and cloud shadows relatively well maintained, which verifies the effectiveness of the proposed algorithm.

### 3.4. Case study: Sentinel-2 image

#### 3.4.1. Experimental setting

The forth real-data experiment was conducted on an image acquired

by the Sentinel-2 sensor over the city of Hangzhou (see Fig. 7(a)). Hangzhou is located in the eastern coastal area of China, and a large amount of rivers are found within the area. Sentinel-2 is a widely used multispectral sensor with 13 spectral channels, which was launched by the European Space Agency in 2015. It has three different spatial resolutions with high quality: 10 m, 20 m, and 60 m. To be consistent with the former experiments, a typical scene of Hangzhou was selected. In this scene, both thick, opaque clouds and thin clouds are included, evenly distributed in the whole image. Bands 1, 2, 3, 8, 11, and 12 were utilized as $B_B$, $B_G$, $B_R$, $B_{NIR}$, $B_{SWIR-1}$, and $B_{SWIR-2}$, respectively. To unify the spatial resolution, bands 1, 2, 3, and 8 were first resampled to have the same spatial resolution as bands 11 and 12. The image scene was then at a size of $5490 \times 5490$, with a spatial resolution of 20 m. The parameters of the proposed CSD-SI algorithm were set as: $T_1 = 1$, $t_2 = 1/10$, $t_3 = 3/4$, $t_4 = 4/5$, $T_5 = 20$, $T_6 = 10$, $T_7 = 3$, and $T_8 = 5$. The reference map and the false-color image for this scene are provided in Fig. 7(b) and Fig. 7(c), respectively.
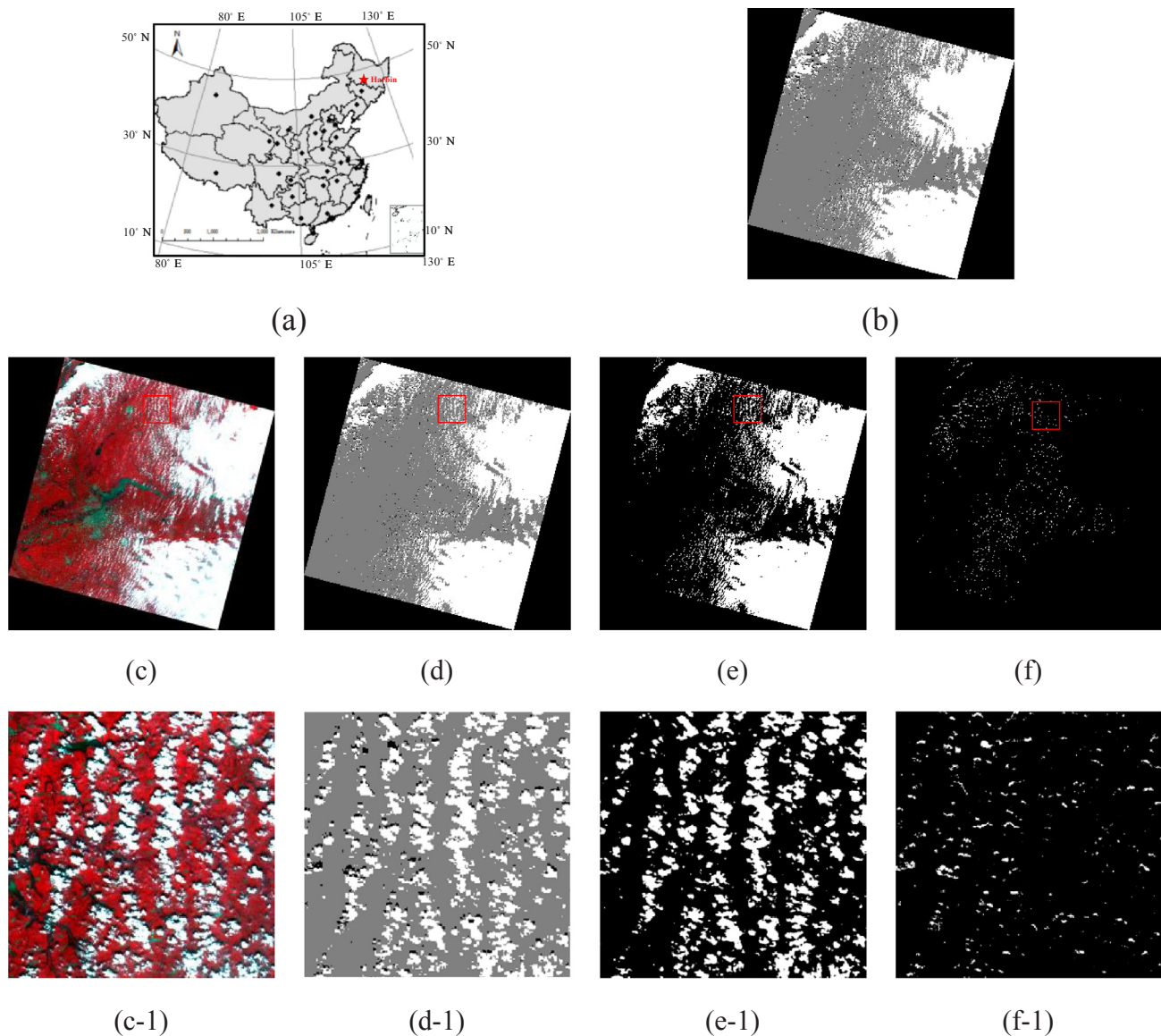
**Fig. 8.** Harbin GF-1 image scene and the cloud/shadow detection results of the proposed CSD-SI detection algorithm: (a) The geographical location of the covered area. (b) The reference map. (c) The false-color composite image of the acquired Harbin GF-1 image scene (R: 4, G: 3, B: 2). (d) The composite cloud/shadow thematic map. (e) The cloud detection map. (f) The cloud shadow detection map. (c-1)–(f-1) Local zoomed maps of the detection results labeled with the red square in (c) to (f). (For interpretation of the references to color in this figure legend, the reader is referred to the web version of this article.)

### 3.4.2. Results

The detection maps of the proposed CSD-SI algorithm are given in Fig. 7(d)–(f). From Fig. 7, it can be seen that the proposed CSD-SI algorithm achieves a relatively good detection performance for this scene. From the whole scene maps and the local zoomed maps, it can be seen that the CSD-SI algorithm effectively detects most of the clouds and their associated shadows, with the edges and details of the clouds and cloud shadows relatively well kept. For the lower-right corner of the image in particular, the details of the clouds and their associated cloud shadows are well maintained. From the composite cloud/shadow thematic map, it can be observed that the detection result is basically consistent with the false-color image. However, it can also be noted that many thin clouds are missed, accounting for approximately 14.58%, especially for the upper part of the image, which limits the detection performance, to some degree.

### 3.5. Case study: GF-1 image

### 3.5.1. Experimental setting

The fifth experiment was conducted using data acquired by the WFV sensor of the GF-1 satellite, which was developed by the Chinese Aerospace Science and Technology Corporation and is a kind of high spatial resolution Earth observation satellite. The GF-1 satellite was launched in 2013, with four multispectral bands at a spatial resolution of 8 m and a panchromatic band at a spatial resolution of 2 m. In this experiment, a typical scene over the city of Harbin at a size of15726 × 15361 was selected. Harbin is located in the northern part of China and has a subtropical climate (see Fig. 8(a)). This scene has a relatively large cloud amount, which is mainly concentrated in the right part of the image, with both thick, opaque clouds and thin clouds included. In addition, only four spectral bands can be accessed, and in the infrared range, only the NIR band is included, which leads to the accessible spectral information being relatively limited, further increasing
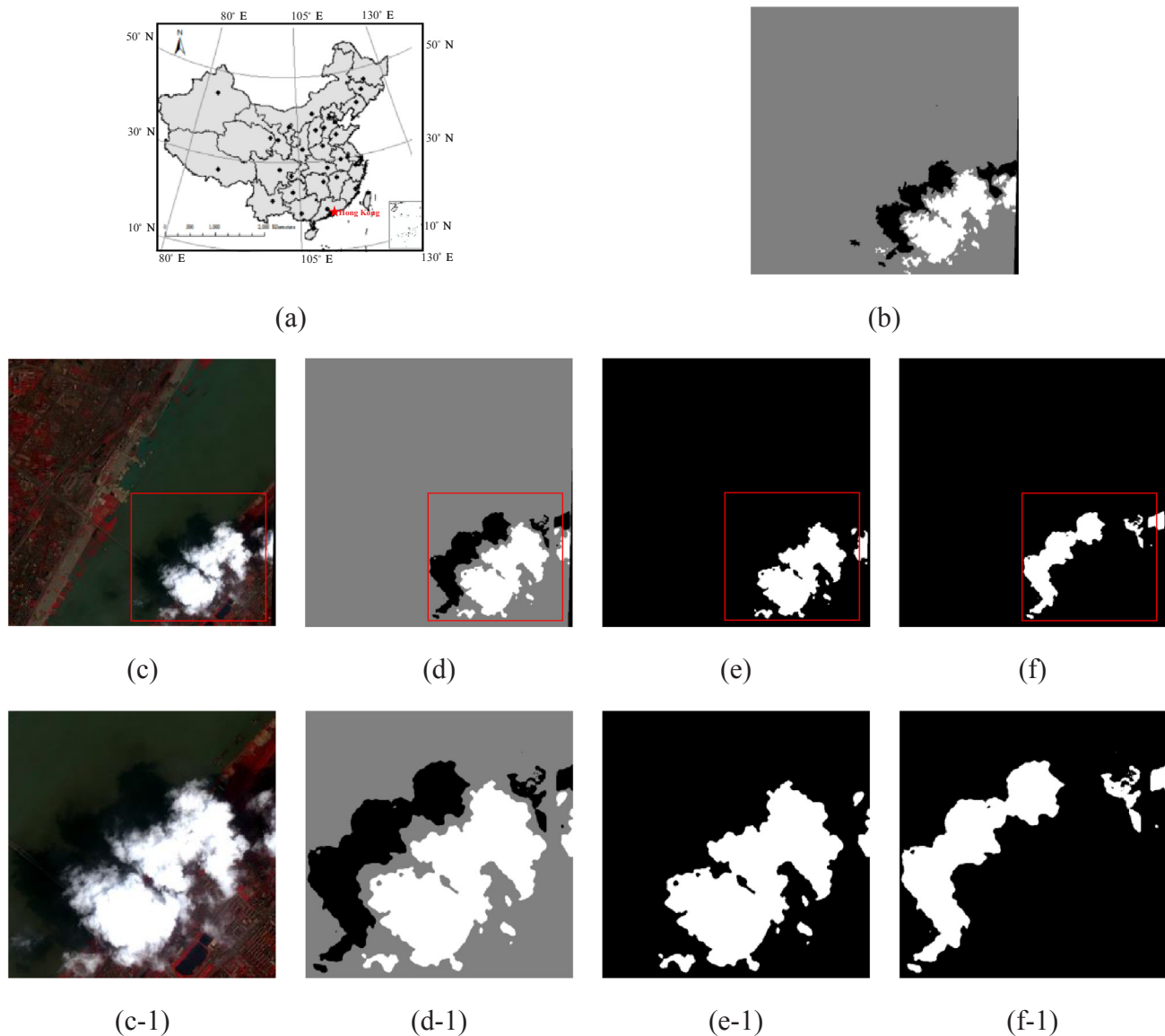
**Fig. 9.** Hong Kong IKONOS image scene and the cloud/shadow detection results of the proposed CSD-SI detection algorithm: (a) The geographical location of the covered area. (b) The reference map. (c) The false-color composite image of the acquired Hong Kong IKONOS image scene (R: 4, G: 3, B: 2). (d) The composite cloud/shadow thematic map. (e) The cloud detection map. (f) The cloud shadow detection map. (c-1)–(f-1) Local zoomed maps of the detection results labeled with the red square in (c) to (f). (For interpretation of the references to color in this figure legend, the reader is referred to the web version of this article.)

the challenge of the cloud/shadow detection. Bands 1, 2, 3, 4, 4, and 4 were utilized as $B_B$, $B_G$, $B_R$, $B_{NIR}$, $B_{SWIR-1}$, and $B_{SWIR-2}$, respectively. The parameters of the proposed CSD-SI algorithm were set as: $T_1 = 1$, $t_2 = 1/3$, $t_3 = 2/3$, $t_4 = 2/3$, $T_5 = 40$, $T_6 = 10$, $T_7 = 9$, and $T_8 = 3$. The reference map and the false-color image for this scene are shown in Fig. 8(b) and Fig. 8(c), respectively.

### 3.5.2. Results

The cloud and cloud shadow detection maps are shown in Fig. 8(d)–(f). From Fig. 8, it can be seen that the proposed CSD-SI algorithm achieves a good performance for this scene, even though the accessible spectral information is very limited. The proposed CSD-SI algorithm effectively detects most of the clouds and their associated shadows, while removing the outliers. In the upper-right part of the image, both the large cloud groups and the small, isolated clouds are relatively well detected. From the whole scene maps, it can be seen that the detection results are basically consistent with the false-color image. From the local zoomed maps, it can be observed that the edges and details of the clouds and cloud shadows are also relatively well kept. In

addition, it is worth mentioning that both the thick, opaque clouds and the thin clouds are well identified in this scene, which further verifies the effectiveness of the proposed algorithm.

### 3.6. Case study: IKONOS image

#### 3.6.1. Experimental setting

The sixth experiment was conducted on another high spatial resolution optical image acquired by the IKONOS sensor, to further test the effectiveness of the proposed CSD-SI algorithm for the four-band high-resolution optical remote sensing sensors. The IKONOS satellite was launched in U.S. in 1999 and was the first commercial high-resolution optical remote sensing satellite. IKONOS has a panchromatic band at a spatial resolution of 1 m and four multispectral bands at a spatial resolution of 4 m. A typical scene over the north of Hong Kong at a size of 1000 × 1000 was selected. Hong Kong is located in the southern coastal area of China (see Fig. 9(a)). This scene differs from the former images, as the cloud/shadow region is mainly found over the river. Therefore, it is a challenging scene for cloud shadow detection because
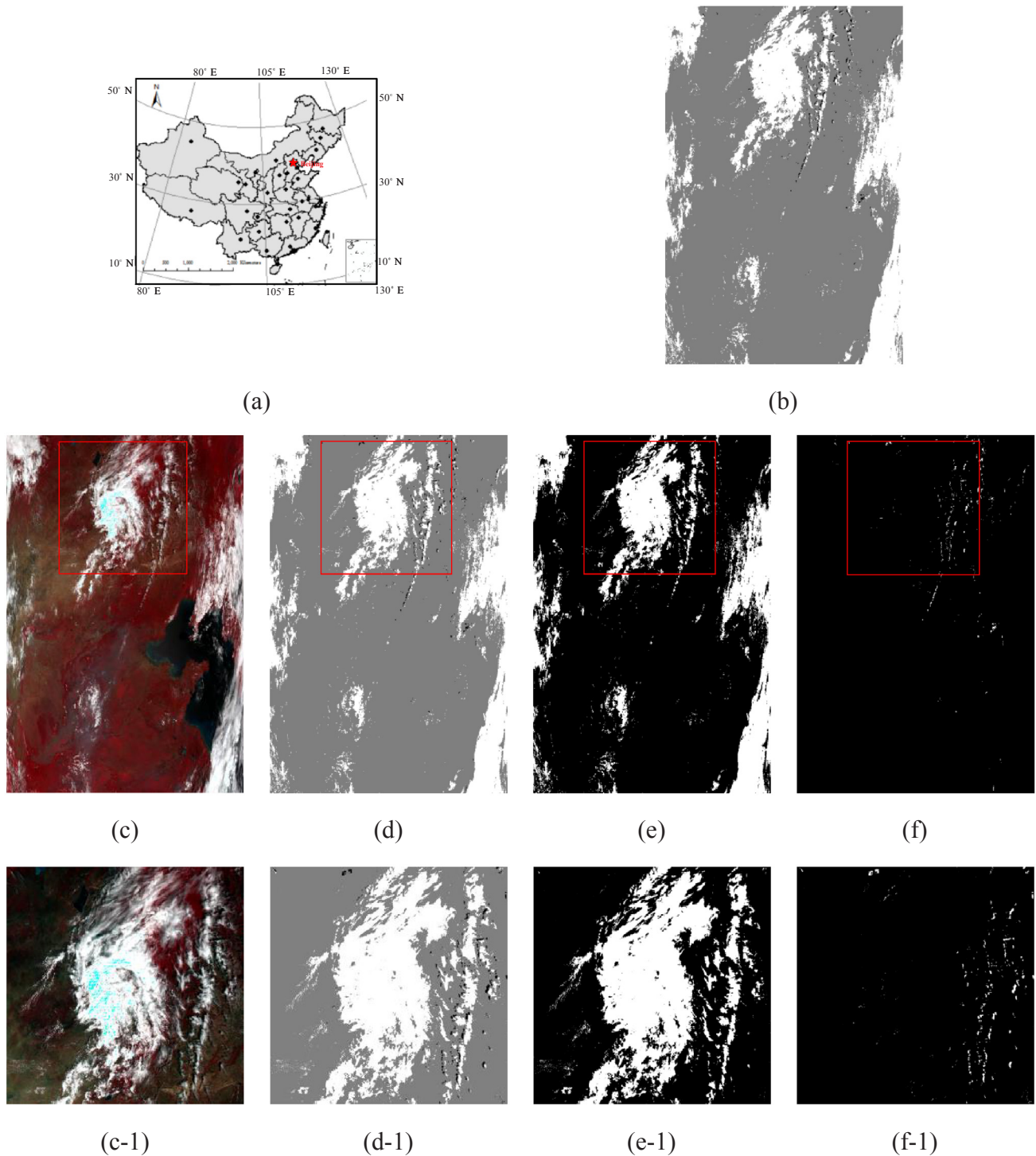
(a)

(b)

(c)          (d)          (e)          (f)

(c-1)          (d-1)          (e-1)          (f-1)

**Fig. 10.** Beijing MODIS image scene and the cloud/shadow detection results of the proposed CSD-SI detection algorithm: (a) The geographical location of the covered area. (b) The reference map. (c) The false-color composite image of the acquired Beijing MODIS image scene (R: 2, G: 1, B: 4). (d) The composite cloud/shadow thematic map. (e) The cloud detection map. (f) The cloud shadow detection map. (c-1)–(f-1) Local zoomed maps of the detection results labeled with the red square in (c) to (f). (For interpretation of the references to color in this figure legend, the reader is referred to the web version of this article.)

of the high similarity between water and cloud shadow. Bands 1, 2, 3, 4, 4, and 4 were utilized as $B_B$, $B_G$, $B_R$, $B_{NIR}$, $B_{SWIR-1}$, and $B_{SWIR-2}$, respectively. The parameters of the proposed CSD-SI algorithm were set as: $T_1 = 1$, $t_2 = 1/6$, $t_3 = 1/2$, $t_4 = 4/5$, $T_5 = 150$, $T_6 = 170$, $T_7 = 7$, and $T_8 = 7$. The reference map and the false-color image for this scene are given in Fig. 9(b) and Fig. 9(c), respectively.

### 3.6.2. Results

The cloud and cloud shadow detection maps are shown in Fig. 9(d)–(f). From Fig. 9, it can be seen that the proposed CSD-SI algorithm performs well, obtaining a relatively good detection result for this scene. From the whole scene maps, it can be seen that both the thick, opaque clouds and most of the thin clouds around the thick clouds are relatively well identified, with most of their associated

shadows, including the parts cast on water, effectively detected. However, some thin clouds and cloud shadows are missed by the proposed CSD-SI algorithm, accounting for approximately 7.33% and 13.96%, respectively. From the local zoomed maps, it can be seen that the detected clouds and cloud shadows are basically consistent with the false-color image, with the edges and the details relatively well maintained.

### 3.7. Case study: MODIS image

#### 3.7.1. Experimental setting

In the seventh real-data experiment, a low spatial resolution hyperspectral image was utilized to evaluate the effectiveness of the proposed CSD-SI algorithm on a hyperspectral sensor. This image was acquired by the MODIS sensor with 36 spectral channels over Beijing. MODIS is one of the most important optical remote sensing sensors for Earth observation, and its data have been widely used in many fields (Xiao et al., 2005; Chen et al., 2007). MODIS provides three low spatial resolutions: 250 m, 500 m, and 1000 m. As in the former experiments, a typical scene at a size of 4080 × 2708 was selected, in which a large part of the image is contaminated by clouds and cloud shadows, with both thick, opaque clouds and thin clouds included. Bands 3, 4, 1, 2, 6, and 7 were utilized as $B_B$, $B_G$, $B_R$, $B_{NIR}$, $B_{SWIR-1}$, and $B_{SWIR-2}$, respectively. The parameters of the proposed CSD-SI algorithm were set as: $T_1 = 1$, $t_2 = 1/10$, $t_3 = 2/3$, $t_4 = 1/2$, $T_5 = 25$, $T_6 = 20$, $T_7 = 3$, and $T_8 = 3$. The reference map for this scene is provided in Fig. 10(b), with the false-color image given in Fig. 10(c).

#### 3.7.2. Results

The detection maps are shown in Fig. 10(d)–(f). From Fig. 10, it can be clearly observed that the proposed CSD-SI algorithm achieves a good detection performance for this scene. Most of the clouds and their associated shadows are effectively identified, with the edges and details relatively well kept, which can be seen from both the whole scene maps and the local zoomed maps. From the composite cloud/shadow thematic map, it can be seen that the detection result is basically consistent with the false-color image.

### 3.8. Case study: Hyperion image

#### 3.8.1. Experimental setting

In order to further test the effectiveness of the proposed CSD-SI algorithm for hyperspectral images, which are very important data resource for remote sensing applications (Zhang et al., 2016; He et al., 2016; He et al., 2017), another hyperspectral dataset acquired by the Hyperion sensor with 240 spectral channels at a moderate resolution of 30 m was utilized to conduct the eighth real-data experiment. Hyperion is an important hyperspectral sensor carried by the Earth Observing-1 (EO-1) satellite and is widely used in various fields. For consistency, a typical scene over the city of Fuzhou at a size of 3421 × 961 was selected. In this scene, the cloud amount is relatively high and the clouds mainly consist of thick, opaque clouds, with most areas covered by clouds and cloud shadows. Bands 14, 22, 32, 50, 146, and 204 were utilized as $B_B$, $B_G$, $B_R$, $B_{NIR}$, $B_{SWIR-1}$, and $B_{SWIR-2}$, respectively. The parameters of the proposed CSD-SI algorithm were set as: $T_1 = 1$, $t_2 = 1/10$, $t_3 = 1/2$, $t_4 = 3/4$, $T_5 = 10$, $T_6 = 30$, $T_7 = 3$, and $T_8 = 3$. The reference map and the false-color image for this scene are provided in Fig. 11(b) and Fig. 11(c), respectively.

#### 3.8.2. Results

The cloud and cloud shadow detection maps are shown in Fig. 11(d)–(f). From the figure, it can be found that the proposed CSD-SI algorithm achieves a good detection performance for this scene. From both the whole scene maps and the local zoomed maps, it can be seen that the detection results are basically consistent with the false-color image, with the edges and details of the clouds and cloud shadows relatively well maintained. Even for the very small clouds close to the large clouds in the middle part of the image, the proposed CSD-SI algorithm performs well.

## 4. Discussion

### 4.1. Algorithm evaluation: The case studies

A number of experiments were conducted to analyze the influence of the eight parameters of the proposed CSD-SI algorithm on the detection performance. To exclude the influence of sensors with different spectral channel settings, five representative experimental images acquired by five different sensors under different situations (i.e., different cloud amounts, different cloud types, and different land covers) were selected, i.e., the Beijing TM image, the Hangzhou Sentinel-2 image, the Hong Kong IKONOS image, the Beijing MODIS image, and the Fuzhou Hyperion image. As the Landsat ETM+ and OLI sensors have similar spectral channel settings to the TM sensor, and the GF-1 sensor is very similar to the IKONOS sensor, they were not utilized in the analysis.

Both PA and UA were utilized to analyze the influence of these parameters on the performance of the proposed CSD-SI algorithm. It should be noted that parameters $T_2$, $T_3$, and $T_4$ are in fact decided by $t_2$, $t_3$, and $t_4$, respectively, according to formulations (5)–(7). Therefore, for convenience, we only need to analyze the influence of $t_2$, $t_3$, and $t_4$ in practice. The PA and UA change trend curves with various values of each parameter under the five different scenes are shown in Fig. 12. A common strategy was utilized, i.e., when analyzing one parameter, the other parameters were fixed at their optimal values.

By comprehensively analyzing Fig. 12, it can be found that parameters $T_2$, $T_3$, and $T_4$ are more sensitive than the other parameters. $T_2$, $T_3$, and $T_4$ are the threshold parameters of the proposed CI and CSI indices for cloud and cloud shadow detection. However, the optimal values of these parameters generally change in a narrow range and can be easily determined for certain image scenes through fine-tuning according to the recommended values of these parameters. The other parameters are less sensitive and the detection performance changes little with the change of these parameters, or is relatively stable in a certain range. In summary, all eight parameters of the proposed CSD-SI algorithm can be easily fine-tuned according to the given formulations and the recommended values in practice. Therefore, CSD-SI does make sense for real applications.

### 4.2. Precision analysis and time consumption for the CSD-SI algorithm

In this section, we compare the mean detection precisions of the proposed CSD-SI algorithm with those of five other state-of-the-art methods: ACCA (Irish et al., 2006), F-mask (Zhu and Woodcock, 2012), F-mask-CDI (Frantz et al., 2018), MLMFF (Bai et al., 2016), and MFC (Li et al., 2017). The results are listed in Table 1.

From the table, it can be seen that although the working mechanism of the proposed CSD-SI algorithm is simple, it can achieve a cloud and cloud shadow detection performance that is comparable with that of the five other state-of-the-art methods. For Landsat series imagery, CSD-SI achieves a competitive cloud and cloud shadow detection performance with regard to the state-of-the-art F-mask algorithm, and it clearly outperforms the ACCA algorithm. Specifically, for cloud, the proposed CSD-SI algorithm achieves a mean PA of 91.83%, which is comparable with the F-mask algorithm, i.e., 92.10%, and is better than the result of the ACCA algorithm, i.e., 72.10%. In addition, the mean UA of the proposed CSD-SI algorithm is 97.61%, which is higher than that of F-mask and ACCA, i.e., 89.40% and 91.8%. For cloud shadow, the ACCA algorithm fails to give a mean evaluation and the F-mask algorithm obtains a PA of 70%+ and a UA of 50%+. Compared with these two algorithms, the proposed CSD-SI algorithm performs better, with the PA and UA both over 80%, which verifies the effectiveness of the proposed algorithm.

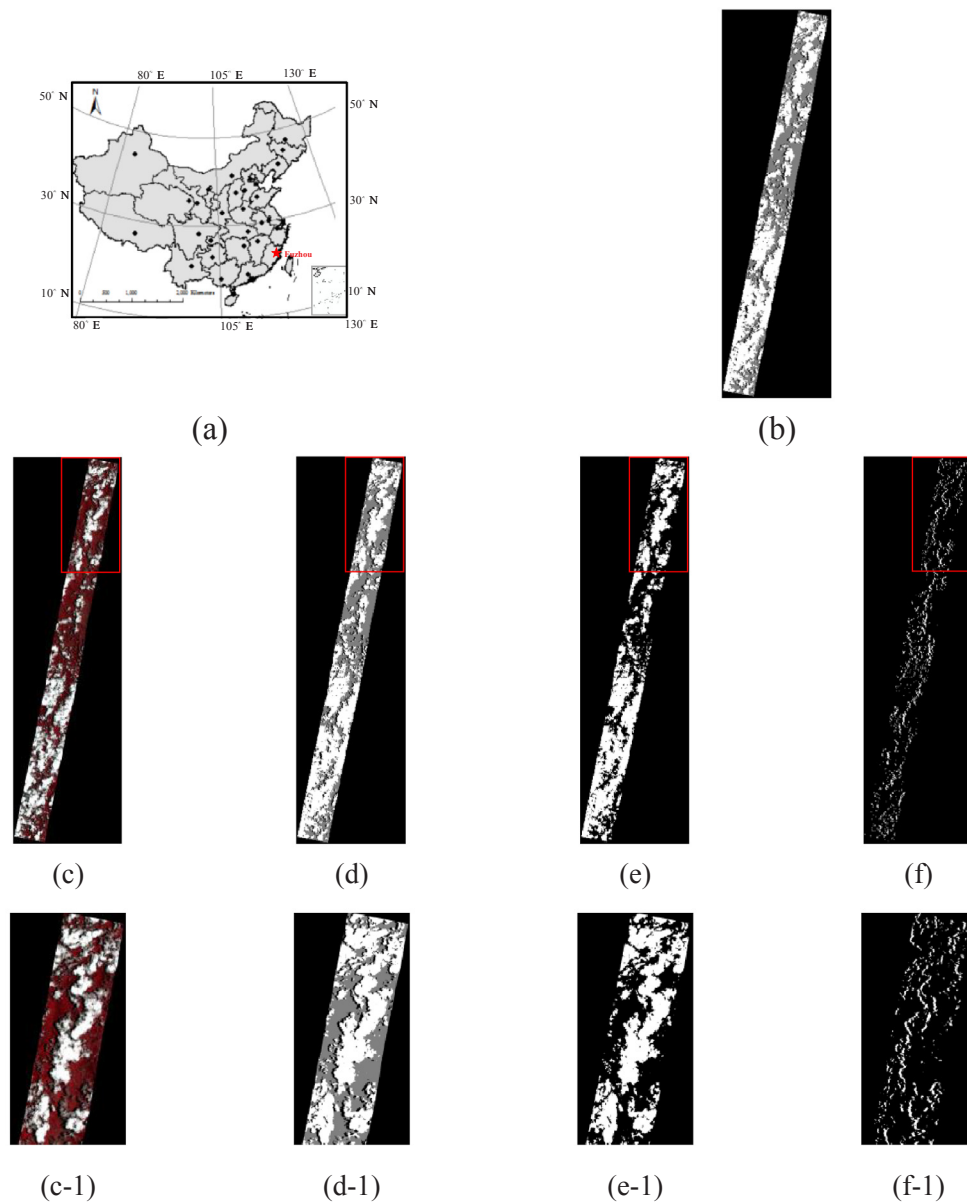For Sentinel 2 image, the proposed CSD-SI algorithm achieves a

**Fig. 11.** Fuzhou Hyperion image scene and the cloud/shadow detection results of the proposed CSD-SI detection algorithm: (a) The geographical location of the covered area. (b) The reference map. (c) The false-color composite image of the acquired Fuzhou Hyperion image scene (R: 50, G: 32, B: 22). (d) The composite cloud/shadow thematic map. (e) The cloud detection map. (f) The cloud shadow detection map. (c-1)–(f-1) Local zoomed maps of the detection results labeled with the red square in (c) to (f). (For interpretation of the references to color in this figure legend, the reader is referred to the web version of this article.)

comparable performance compared with the state-of-the-art F-mask-CDI algorithm. Specifically, for cloud, it achieves a higher OA of 97.24% and higher UA of 98.32% than that of F-mask-CDI, and a lower PA of 85.42% compared with the values of F-mask-CDI. For cloud shadow, the proposed CSD-SI achieves a PA of 82.67% and a UA of 81.37%, while F-mask-CDI does not give a mean evaluation as it is specifically designed for cloud detection.

Similarly, for the GF-1 image, the proposed CSD-SI algorithm achieves a comparable performance when compared with the state-of-the-art MLMFF and MFC algorithms. Specifically, for cloud, it achieves an OA of 99.31%, with a PA and UA of 98.23% and 99.22%, respectively, which are higher than the values obtained by the MLMFF and MFC algorithms. For cloud shadow, it achieves a PA of 79.99% and a UA of 91.64%, which are higher than the values obtained by the MFC algorithm. MLMFF fails to give a mean evaluation for cloud shadow as it is specifically designed for cloud detection. It is worth mentioning that for the other high spatial resolution optical sensor, i.e., IKONOS,

the proposed CSD-SI algorithm again achieves a good performance, which further confirms its effectiveness for high-resolution optical sensors. Specifically, for the IKONOS image, it achieves an OA of 99.27%, a PA of 92.67%, and a UA of 95.44% for cloud. Meanwhile, for cloud shadow, it achieves a PA of 86.04% and a UA of 85.49%.

The mean quantitative evaluation results of the cloud and cloud shadow detection results of all eight widely used optical remote sensing sensors are given in Table 1. It can be seen from the table that the proposed CSD-SI algorithm generally achieves comparable OA, UA, and PA values. Specifically, for cloud, it achieves a mean PA and a mean UA of 93.13% and 98.13%, respectively, and for cloud shadow, it achieves a mean PA of 84.33% and a mean UA of 89.12%, which are at relatively high levels. Overall, it can be concluded that the proposed CSD-SI algorithm is an effective multi-source cloud and cloud shadow detection method for most of the widely used optical sensors with both visible and infrared spectral channels. From this perspective, it makes sense for practical remote sensing applications.
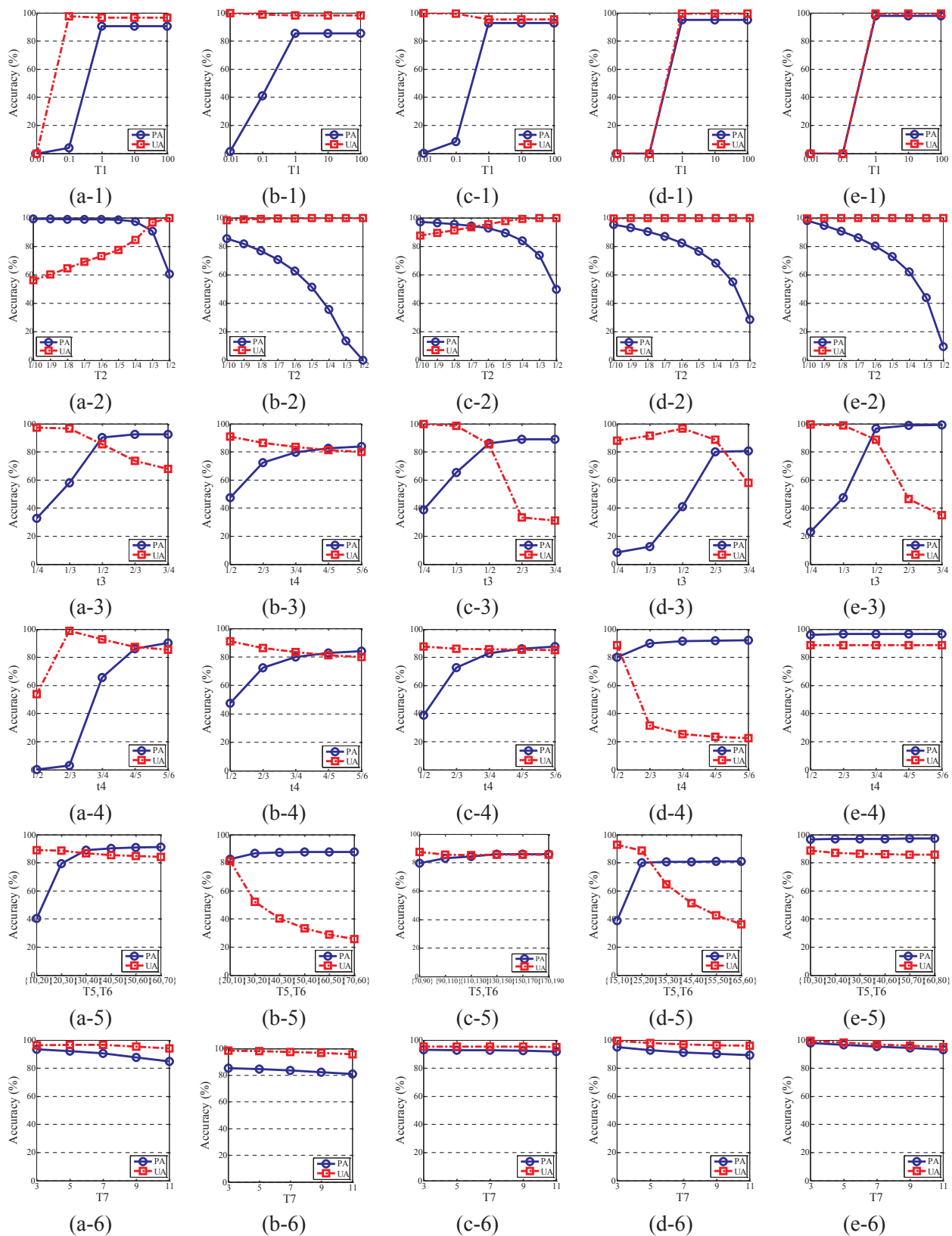
**Fig. 12.** The producer's accuracy (PA) and user's accuracy (UA) versus each parameter of the proposed CSD-SI algorithm for the five different scenes, with the first row, second row, third row, fourth row, fifth row, sixth row, and seventh row denoting the sensitivity analysis of parameters $T_1$, $t_2$, $t_3$, $t_4$, $T_5$ and $T_6$, $T_7$, $T_8$, respectively. (a) Beijing TM image scene. (b) Hangzhou Sentinel-2 image scene. (c) Hong Kong IKONOS image scene. (d) Beijing MODIS image scene. (e) Fuzhou Hyperion image scene.

**Table 1**
Mean cloud and cloud shadow detection precisions of the different cloud/shadow detection methods (Zhu and Woodcock, 2012; Li et al., 2017; Bai et al., 2016; Frantz, et al., 2018).

| Sensor | Method | Type | Overall accuracy (%) | Producer's accuracy (%) | User's accuracy (%) |
|---|---|---|---|---|---|
| Landsat 7 ETM+ | ACCA | Cloud | 84.8 | 72.1 | 91.8 |
| | | Cloud shadow | – | – | – |
| Landsat | F-mask | Cloud | 96.41 | 92.10 | 89.40 |
| | | Cloud shadow | – | > 70 | > 50 |
| Landsat | CSD-SI | Cloud | 97.92 | 91.83 | 97.61 |
| | | Cloud shadow | – | 83.07 | 92.36 |
| Sentinel-2 | F-mask-CDI | Cloud | 95.00 | 99.00 | 93.00 |
| | | Cloud shadow | – | – | – |
| Sentinel-2 | CSD-SI | Cloud | 97.24 | 85.42 | 98.32 |
| | | Cloud shadow | – | 82.67 | 81.37 |
| GF-1 | MFC | Cloud | 98.30 | 88.78 | 94.36 |
| | | Cloud shadow | – | 74.66 | 74.48 |
| GF-1 | MLMFF | Cloud | > 91.45 | 93.67 | 95.67 |
| | | Cloud shadow | – | – | – |
| GF-1 | CSD-SI | Cloud | 99.31 | 98.23 | 99.22 |
| | | Cloud shadow | – | 79.99 | 91.64 |
| All eight optical sensors | CSD-SI | Cloud | 98.52 | 93.13 | 98.13 |
| | | Cloud shadow | – | 84.33 | 89.12 |

**Table 2**
The running times for the eight different optical sensor image scenes.

| Image scene no. | 1 | 2 | 3 | 4 | 5 | 6 | 7 | 8 |
|---|---|---|---|---|---|---|---|---|
| Spectral tests (sec) | 41.35 | 43.51 | 55.19 | 11.82 | 59.79 | 0.82 | 3.65 | 1.33 |
| Spatial matching (min) | 39.81 | 40.66 | 50.83 | 5.80 | 70.53 | 13.70 | 0.31 | 1.29 |
| Total time (min) | 40.50 | 41.39 | 51.75 | 6.00 | 71.53 | 13.71 | 0.37 | 1.31 |

1: Landsat 5 TM image scene; 2: Landsat 7 ETM+ image scene; 3: Landsat 8 OLI image scene; 4: Sentinel 2 image scene; 5: GF-1 image scene; 6: IKONOS image scene; 7: MODIS image scene; 8: Hyperion image scene.

We now come to the time consumption analysis for the proposed CSD-SI algorithm. The time consumption of the proposed CSD-SI algorithm is relatively low, owing to its simple working mechanism. CSD-SI consists of two main steps: the spectral index tests and the spatial matching refinement. The experimental program was coded in MATLAB on a personal computer with an Intel Core i7-6700HU CPU and 12 GB of memory. The detailed running times for all eight optical sensors, including the spectral test time, the spatial matching time, and the total time, are listed in Table 2.

From Table 2, it can be seen that the first step, the spectral index tests, is very fast and only needs a few seconds for the whole large image scenes, whereas the second step, spatial matching refinement, is relatively time-consuming. Depending on the image size and the size of the local search window, the time for this step varies from several minutes to dozens of minutes. All in all, the time consumption of the proposed CSD-SI algorithm is relatively low, owing to its simple mechanism. In addition, for real applications, the proposed CSD-SI algorithm could be implemented in C++ code with the parallel computing

**Table 3**
The quantitative evaluation of the precision of the proposed CSD-SI algorithm for the eight different optical sensor image scenes with different spectral and spatial resolution levels.

| Sensor | Image scene | Type | Overall accuracy (%) | Producer's accuracy (%) | User's accuracy (%) |
|---|---|---|---|---|---|
| Landsat5 TM | Beijing | Cloud | 99.72 | 90.70 | 96.69 |
| | | Cloud shadow | – | 90.31 | 85.49 |
| Landsat7 ETM+ | Taiyuan | Cloud | 99.79 | 95.18 | 97.06 |
| | | Cloud shadow | – | 80.53 | 96.98 |
| Landsat8 OLI | Kunming | Cloud | 94.24 | 89.61 | 99.07 |
| | | Cloud shadow | – | 78.38 | 94.60 |
| Sentinel-2 | Hangzhou | Cloud | 97.24 | 85.42 | 98.32 |
| | | Cloud shadow | – | 82.67 | 81.37 |
| GF-1 WFV | Harbin | Cloud | 99.31 | 98.23 | 99.22 |
| | | Cloud shadow | – | 79.99 | 91.64 |
| IKONOS | Hong Kong | Cloud | 99.27 | 92.67 | 95.44 |
| | | Cloud shadow | – | 86.04 | 85.49 |
| MODIS | Beijing | Cloud | 98.90 | 95.14 | 99.56 |
| | | Cloud shadow | – | 80.14 | 88.57 |
| Hyperion | Fuzhou | Cloud | 99.67 | 98.07 | 99.67 |
| | | Cloud shadow | – | 96.54 | 88.79 |

technique to accelerate the computation speed, which would further decrease the running time to a large degree.

### 4.3. Performance evaluation: The case studies

In this section, we comprehensively analyze the performance of the proposed CSD-SI algorithm and compare the detection performance in the different case studies both qualitatively and quantitatively, with the quantitative assessments of the eight experiments provided in Table 3.

For the first two multispectral image scenes, i.e., the Landsat 5 TM Beijing image scene and the Landsat 7 ETM+ Taiyuan image scene, in which the clouds mainly consist of thick, opaque clouds, the proposed CSD-SI algorithm performs well and achieves good detection results. It effectively detects most of the clouds and cloud shadows and relieves the disturbances caused by other land materials with similar spectral responses, owing to the effectiveness of the proposed CI and CSI indices and the spatial matching strategy. Specifically, for cloud, it achieves PA values of 90.70% and 95.18% and UA values of 96.96% and 97.06% for the Beijing TM image and Taiyuan ETM+ image, respectively, which suggests that both the omission rate and commission rate are relatively low. For cloud shadow, the proposed CSD-SI algorithm achieves a PA of 90.31% and a UA of 85.49% for the Beijing TM image and achieves a PA of 80.53% and a UA of 96.98% for the Taiyuan ETM+ image, which can also be considered as good results.

Compared with the two former multispectral image scenes, the cloud detection precisions for the Landsat 8 OLI Kunming image scene and the Sentinel-2 Hangzhou image scene are relatively low. Many thin clouds around the thick, opaque clouds in these two scenes are not effectively detected, due to the limited detection capability of the proposed CI index for very thin clouds. Specifically, for cloud, the proposed CSD-SI algorithm achieves PA values of 89.61% and 85.42% for the Kunming OLI image and Hangzhou Sentinel-2 image, respectively. The UA values for cloud are again at a high level, i.e., 99.07% and 98.32%, which means that few pixels of other land materials are

misclassified as cloud. For cloud shadow, the detection precisions are lower compared with the previous two experimental images, as the serious disturbances caused by the topographical shadows make the cloud shadow detection more challenging. Specifically, the proposed CSD-SI algorithm achieves PA values of 78.38% and 82.67% and UA values of 94.60% and 81.37% for the Kunming OLI image and Hangzhou Sentinel-2 image, respectively. Overall, the detection precisions for cloud and cloud shadow in these two scenes can still be considered as acceptable.

We now turn to the experimental results obtained with the two four-band high-resolution optical remote sensing image scenes, i.e., the Harbin GF-1 WFV image scene and the Hong Kong IKONOS image scene. It can be found that the proposed CSD-SI algorithm again works well and achieves good detection results with relatively high detection precisions for these two image scenes, even though the accessible spectral information is very limited. For cloud, most of the thick, opaque clouds and the thin clouds around them are accurately detected, with the disturbances well removed, which further illustrates the effectiveness of the proposed CI index. Meanwhile, the cloud shadows are also well detected. It is worth mentioning that, for the Hong Kong IKONOS image scene, most of the cloud shadows are cast on the river, which results in a very challenging task for cloud shadow detection, due to the similar spectral characteristics of water and cloud shadow. It can be found that most of the cloud shadows are well separated from the water, which further shows the effectiveness of the proposed CSI index and the spatial matching strategy. Specifically, the CSD-SI algorithm achieves PA and UA values of 98.23% and 99.22% for cloud and 79.99% and 91.64% for cloud shadow for the Harbin GF-1 WFV image, with the PA and UA values being 92.67% and 95.44% for cloud and 86.04% and 85.49% for cloud shadow for the Hong Kong IKONOS image. In summary, the proposed CSD-SI algorithm can also be effectively applied to the four-band high-resolution optical remote sensing sensors.

For the last two experiments conducted on hyperspectral sensor image scenes, i.e., the Beijing MODIS image scene and the Fuzhou Hyperion image scene, it can be found that the proposed CSD-SI algorithm again performs well and achieves a relatively good performance by accurately detecting most of the clouds and cloud shadows and effectively removing the disturbances. Specifically, for cloud, it achieves PA values of 95.14% and 98.07% and UA values of 99.56% and 99.67% for the Beijing MODIS image scene and the Fuzhou Hyperion image scene, respectively, which are at a relatively high level in practice. For cloud shadow, it achieves PA values of 80.14% and 96.54% and UA values of 88.57% and 88.79% for the Beijing MODIS image scene and the Fuzhou Hyperion image scene, respectively. In summary, the results of these two experiments suggest that the proposed CSD-SI algorithm can also be effectively applied to hyperspectral sensors.

By comprehensively analyzing the results of the eight experiments, it can be concluded that the proposed CSD-SI algorithm can be considered as a unified method for various kinds of widely used optical remote sensing sensors with both visible and infrared bands, including both multispectral and hyperspectral sensors, and low-resolution and high-resolution sensors, which proves its effectiveness and generalizability. From this perspective, the proposed CSD-SI algorithm makes sense for practical remote sensing applications.

## 5. Conclusion

In this paper, we have proposed a unified cloud/shadow detection algorithm based on spectral indices (CSD-SI) for multi/hyperspectral optical remote sensing sensors with both visible and infrared spectral channels. Based on the spectral reflective characteristics of cloud and cloud shadow, the CI and CSI indices are proposed to indicate the potential clouds and cloud shadows, respectively. Considering the spatial coexistence between clouds and their associated shadows, a spatial matching strategy is further utilized to refine the cloud shadow

detection result, which can effectively screen out the outliers caused by topographical shadows and other dark land materials. Eight different types of multi/hyperspectral optical remote sensing images with various cloud types and cloud amounts in different geographical environments were utilized to demonstrate the effectiveness of the proposed CSD-SI algorithm. The results clearly show that the proposed CSD-SI algorithm is, indeed, a unified cloud/shadow detection method which can work well for various types of optical sensors with both visible and infrared spectral channels, including both multispectral and hyperspectral sensors with various spatial resolution levels.

However, there is still some room for improvement of the proposed algorithm. For thin cirrus clouds, the performance of the proposed CSD-SI algorithm is limited. In addition, the cloud shadow detection capability could be further improved by combining the proposed CSD-SI algorithm with a geometrical method to better separate cloud shadows from water. All of these issues will be addressed in our future work.

## References

Bai, T., Li, D., Sun, K., Chen, Y., Li, W., 2016. Cloud detection for high-resolution satellite imagery using machine learning and multi-feature fusion. Remote Sensing 8 (9), 715.
Clerbaux, C., Boynard, A., Clarisse, L., George, M., Hadji-Lazaro, J., Herbin, H., Wespes, C., 2009. Monitoring of atmospheric composition using the thermal infrared IASI/MetOp sounder. Atmos. Chem. Phys. 9 (16), 6041–6054.
Chen, Z., Hu, C., Muller-Karger, F., 2007. Monitoring turbidity in Tempa Bay using MODIS/Aqua 250-m imagery. Remote Sens. Environ. 109 (2), 207–220.
Dozier, J., 1989. Spectral signature of alpine snow cover from the Landsat Thematic Mapper. Remote Sens. Environ. 28, 9–22.
DeFries, R.S., Townshend, J.R.G., 1994. NDVI-derived land cover classification at a global scale. Remote Sens. Environ. 15 (17), 3567–3586.
Frantz, D., Haß, E., Uhl, A., Stoffels, J., Hill, J., 2018. Improvement of the F-mask algorithm for Sentinel-2 images: separating clouds from bright surfaces based on parallax effects. Remote Sens. Environ. https://doi.org/10.1016/j.rse.2018.04.046.
Goodwin, N.R., Collett, L.J., Denham, R.J., Flood, N., Tindall, D., 2013. Cloud and cloud shadow screening across Queensland, Australia: An automated method for Landsat TM/ETM+ time series. Remote Sens. Environ. 134, 50–65.
Goward, S.N., Markham, B., Dye, D.G., Dulaney, W., Yang, J., 1991. Normalized difference vegetation index measurements from the Advanced Very High Resolution Radiometer. Remote Sens. Environ. 35 (2), 257–277.
Gao, B.C., 1996. NDWI-A normalized difference water index for remote sensing of vegetation liquid water from space. Remote Sens. Environ. 58 (3), 257–266.
Hughes, M., Hayes, D., 2014. Automated detection of cloud and cloud shadow in single-date Landsat imagery using neural networks and spatial post-processing. Remote Sensing 6, 4907–4926.
Huang, C., Thomas, N., Goward, S.N., Masek, J.G., Zhu, Z., Townshend, J.R., et al., 2010a. Automated masking of cloud and cloud shadow for forest change analysis using Landsat images. Int. J. Remote Sens. 31 (20), 5449–5464.
He, W., Zhang, H., Zhang, L., Shen, H., 2016. Total-variation-regularized low-rank matrix factorization for hyperspectral image restoration. IEEE Trans. Geosci. Remote Sens. 54 (1), 178–188.
He, W., Zhang, H., Zhang, L., 2017. Total variation regularized reweighted sparse nonnegative matrix factorization for hyperspectral unmixing. IEEE Trans. Geosci. Remote Sens. 55 (7), 3909–3921.
Huang, C., Goward, S.N., Masek, J.G., Thomas, N., Zhu, Z., Vogelmann, J.E., 2010b. An automated approach for reconstructing recent forest disturbance history using dense Landsat time series stacks. Remote Sens. Environ. 114, 183–198.
Irish, R.R., Barker, J.L., Goward, S.N., Arvidson, T., 2006. Characterization of Landsat7 ETM+ automated cloud-cover assessment (ACCA) algorithm. Photogramm. Eng. Remote Sens. 72 (10), 1179.
Ishida, H., Oishi, Y., Morita, K., Moriwaki, K., Nakajima, T.Y., 2018. Development of a

support vector machine based cloud detection method for MODIS with the adjust-ability to various conditions. Remote Sens. Environ. 205, 390–407.

Jin, S., Homer, C., Yang, L., Xian, G., Fry, J., Danielson, P., et al., 2013. Automated cloud and shadow detection and filling using two-data Landsat imagery in the USA. Int. J. Remote Sens. 34 (5), 1540–1560.

Kauth, R.J., Thomas, G.S., 1976. The tasselled cap-a graphic description of the spectral-temporal development of the agricultural crops as seen by Landsat. Proceedings of the Symposium on Machine Processing of Remotely Sensed Data. Purdue University, West Lafayette, Indiana, USA pp. 4B41–4B50.

Kennedy, R.E., Yang, Z., Cohen, W.B., 2010. Detecting trends in forest disturbance and recovery using Landsat time series: 1. LandTrendr-Temporal segmentation algorithm. Remote Sens. Environ. 114 (12), 2897–2910.

Lu, Y., Coops, N.C., Hermosilla, T., 2017. Estimating urban vegetation fraction across 25 cities in pan-Pacific using Landsat time series data. ISPRS J. Photogramm. Remote Sens. 126, 11–23.

Lin, C.H., Lin, B.Y., Lee, K.Y., Chen, Y.C., 2015. Radiometric normalization and cloud detection of optical satellite images using invariant pixels. ISPRS J. Photogramm. Remote Sens. 106, 107–117.

Le Hégarat-Mascle, S., André, C., 2009. Use of Markov random fields for automatic cloud/shadow detection on high resolution optical images. ISPRS J. Photogramm. Remote Sens. 64, 351–366.

Li, H., Zheng, H., Han, C., Wang, H., Miao, H., 2018. Onboard spectral ad spatial cloud detection for hyperspectral remote sensing images. Remote Sensing 10 (1), 152.

Li, P., Dong, L., Xiao, H., Xu, M., 2015. A cloud image detection method based on SVM vector machine. Neurocomputing 169, 34–42.

Li, S., Sun, D., Yu, Y., 2013. Automatic cloud-shadow removal from flood/standing water maps using MSG/SEVIRI imagery. Int. J. Remote Sens. 34 (15), 5487–5502.

Li, Z., Shen, H., Li, H., Xia, G., Gamaba, P., Zhang, L., 2017. Multi-feature combined cloud and cloud shadow detection in GF-1 WMF imagery over land. Remote Sens. Environ. 191, 342–358.

Luo, Y., Trishchenko, A.P., Khlopenkov, K.V., 2008. Developing clear-sky, cloud and cloud shadow mask for producing clear-sky composites at 250-meter spatial resolu-tion for the seven MODIS land bands over Canada and North America. Remote Sens. Environ. 112, 4167–4185.

McFeeters, S.K., 1996. The use of the Normalized Difference Water Index (NDWI) in the delineation of open water features. Int. J. Remote Sens. 17 (7), 1425–1432.

Platnick, S., King, M.D., Ackerman, S.A., Menzel, W.P., Baum, B.A., Riedi, J.C., Frey, R.A., 2003. The MODIS cloud products: Algorithms and examples from Terra. IEEE Trans. Geosci. Remote Sens. 41 (2), 459–473.

Qiu, S., He, B.B., Zhu, Z., Liao, Z.M., Quan, X.W., 2017. Improving F-mask cloud and cloud shadow detection in mountainous area for Landsat 4–8 images. Remote Sens. Environ. 199, 107–119.

Richter, R., Muller, A., 2005. De-shadowing of satellite/airborne imagery. Int. J. Remote

Sens. 26 (15), 3137–3148.

Roy, D.P., Ju, J., Kline, K., Scaramuzza, P.L., Kovalskyy, V., Hansen, M., et al., 2010. Webenabled Landsat data (WELD): Landsat ETM+ composited mosaics of con-terminous United States. Remote Sens. Environ. 114 (1), 35–49.

Sun, L., Mi, X., Wei, J., Wang, J., Tian, X., Yu, H., Gan, P., 2017. A cloud detection algorithm-generating method for remote sensing data at visible to short-wave in-frared wavelength. ISPRS J. Photogramm. Remote Sens. 124, 70–88.

Sun, L., Liu, X., Yang, Y., Chen, T., Wang, Q., Wang, Q., 2018. A cloud shadow detection method combined with cloud height iteration and spectral analysis for Landsat8 OLI data. ISPRS J. Photogramm. Remote Sens. 138, 193–207.

Simpson, J.J., Stitt, J.R., 1998. A procedure for the detection and removal of cloud shadow from AVHRR data over land. IEEE Trans. Geosci. Remote Sens. 36 (3), 880–897.

Tucker, C.J., Pinzon, J.E., Brown, M.E., Slayback, D.A., Pak, E.W., Mahoney, R., EI Saleous, N., 2005. An extended AVHRR 8-km NDVI dataset compatible with MODIS and SPOT vegetation NDVI data. Int. J. Remote Sens. 26 (20), 4485–4498.

Vivone, G., Addesso, P., Conte, R., Longo, M., Restaino, R., 2014. A class of cloud de-tection algorithms based on a map-mrf approach in space and time. IEEE Trans. Geosci. Remote Sens. 52, 5100–5115.

Wu, T., Hu, X., Zhang, Y., Zhang, L., Tao, P., Lu, L., 2016. Automatic cloud detection for high resolution stereo images and its application in terrain extraction. ISPRS J. Photogramm. Remote Sens. 121, 143–156.

Xiao, X., Boles, S., Liu, J., Zhuang, D., Frolking, S., Li, C., Moore, B., 2005. Mapping paddy rice agriculture in southern China using multi-temporal MODIS images. Remote Sens. Environ.

Zhu, Z., Woodcock, C.E., 2012. Object-based cloud and cloud shadow detection in Landsat imagery. Remote Sens. Environ. 118 (15), 83–94.

Zhu, Z., Wang, S.X., Woodcock, C.E., 2015. Improvement and expansion of the F-mask algorithm: cloud, cloud shadow, and snow detection for Landsats 4–7, 8, and Sentinel 2 images. Remote Sens. Environ. 159, 269–277.

Zhu, Z., Woodcock, C.E., 2014. Automated cloud, cloud shadow, and snow detection based on multitemporal Landsat data: an algorithm specifically designed for land cover change. Remote Sens. Environ. 152, 217–234.

Zhu, Z., 2017. Change detection using Landsat time series: a review of frequencies, pre-processing, algorithms, and applications. ISPRS J. Photogramm. Remote Sens. 130, 370–384.

Zhang, Y., Guindon, B., Cihlar, J., 2002. An image transform to characterize and com-pensate for spatial variations in thin cloud contamination of Landsat images. Remote Sens. Environ. 82, 173–187.

Zhang, H., Zhai, H., Zhang, L., Li, P., 2016. Spectral-Spatial Sparse Subspace Clustering for Hyperspectral Remote Sensing Images. IEEE Trans. Geosci. Remote Sens. 54 (6), 3672–3684.